

# Pattern completion and disruption characterize contextual modulation in mouse visual cortex

Jiakun Fu<sup>1,2</sup>, Suhas Shrinivasan<sup>3</sup>, Kayla Ponder<sup>1,2</sup>, Taliah Muhammad<sup>1,2</sup>, Zhuokun Ding<sup>1,2</sup>, Eric Wang<sup>1,2</sup>, Zhiwei Ding<sup>1,2</sup>, Dat T. Tran<sup>1,2</sup>, Paul G. Fahey<sup>1,2</sup>, Stelios Papadopoulos<sup>1,2</sup>, Saamil Patel<sup>1,2</sup>, Jacob Reimer<sup>1,2</sup>, Alexander S. Ecker<sup>3,4</sup>, Xaq Pitkow<sup>1,2</sup>, Ralf M. Haefner<sup>5</sup>, Fabian H. Sinz<sup>1,2,3,6</sup>, Katrin Franke<sup>1,2,†,✉</sup>, and Andreas S. Tolias<sup>1,2,†,✉</sup>

<sup>1</sup>Department of Neuroscience, Baylor College of Medicine, Houston, Texas, USA

<sup>2</sup>Center for Neuroscience and Artificial Intelligence, Baylor College of Medicine, Houston, TX, USA

<sup>3</sup>Institute of Computer Science and Campus Institute Data Science, University of Göttingen, Germany

<sup>4</sup>Max Planck Institute for Dynamics and Self-Organization, Göttingen, Germany

<sup>5</sup>Brain and Cognitive Sciences, Center for Visual Science, University of Rochester, Rochester, USA

<sup>6</sup>Institute for Bioinformatics and Medical Informatics, University of Tübingen, Tübingen, Germany

† Senior authors

A key role of sensory processing is integrating information across space. Neuronal responses in the visual system are influenced by both local features in the receptive field center and contextual information from the surround. While center-surround interactions have been extensively studied using simple stimuli like gratings, investigating these interactions with more complex, ecologically-relevant stimuli is challenging due to the high dimensionality of the stimulus space. We used large-scale neuronal recordings in mouse primary visual cortex to train convolutional neural network (CNN) models that accurately predicted center-surround interactions for natural stimuli. These models enabled us to synthesize surround stimuli that strongly suppressed or enhanced neuronal responses to the optimal center stimulus, as confirmed by *in vivo* experiments. In contrast to the common notion that congruent center and surround stimuli are suppressive, we found that excitatory surrounds appeared to complete spatial patterns in the center, while inhibitory surrounds disrupted them. We quantified this effect by demonstrating that CNN-optimized excitatory surround images have strong similarity in neuronal response space with surround images generated by extrapolating the statistical properties of the center, and with patches of natural scenes, which are known to exhibit high spatial correlations. Our findings cannot be explained by theories like redundancy reduction or predictive coding previously linked to contextual modulation in visual cortex. Instead, we demonstrated that a hierarchical probabilistic model incorporating Bayesian inference, and modulating neuronal responses based on prior knowledge of natural scene statistics, can explain our empirical results. We replicated these center-surround effects in the multi-area functional connectomics MICrONS dataset using natural movies as visual stimuli, which opens the way towards understanding circuit level mechanism, such as the contributions of lateral and feedback recurrent connections. Our data-driven modeling approach provides a new understanding of the role of contextual interactions in sensory processing and can be adapted across brain areas, sensory modalities, and species.

Correspondence: [astolias@bcm.edu](mailto:astolias@bcm.edu), [katrin.franke@bcm.edu](mailto:katrin.franke@bcm.edu)

## Introduction

Across animal species, sensory information is processed in a context-dependent manner and, therefore, the perception of a specific stimulus varies with context. This mechanism allows to flexibly adjust sensory processing to changing envi-

ronments and tasks. In vision, context is provided by global aspects of the visual scene. For example, reliable object detection not only depends on integrating local object features like contours or textures, but also on the visual scene surrounding the object (Biederman et al., 1982; Hock et al., 1974). Physiologically, this is reflected by the fact that responses of visual neurons to stimuli presented in their receptive field (RF) center (i.e. classical RF) — the region of space in which visual stimuli evoke responses — are modulated by stimuli presented in their RF surround (i.e. extra-classical RF). This center-surround contextual modulation has been described across several processing levels of the visual system, from the retina to visual cortex (Chiao and Masland, 2003; Goldin et al., 2022; Alitto and Usrey, 2008; Knierim and Van Essen, 1992; Keller et al., 2020b; Jones et al., 2012; Rossi et al., 2001; Vinje and Gallant, 2000), and is mediated by both lateral interactions and feedback from higher visual areas (Nassi et al., 2013; Nurminen et al., 2018; Keller et al., 2020a; Shen et al., 2022; Adesnik et al., 2012).

How context modulates visual activity has so far largely been studied in non-ecological settings with well-interpretable parametric stimuli, like oriented gratings. Studies in non-human primates, and more recently mice (Keller et al., 2020a; Self et al., 2014; Samonds et al., 2017; Keller et al., 2020b), have provided important insights into center-surround modulations in the primary visual cortex (V1). The most commonly observed center-surround modulation is suppression, where neuronal responses to stimuli presented in the center RF decrease in the presence of certain surrounding stimuli (Knierim and Van Essen, 1992; Levitt and Lund, 1997; Kapadia et al., 1999; Sceniak et al., 1999; Cavanaugh et al., 2002b,c; Nassi et al., 2013; Nurminen et al., 2018). The strength of the suppression tends to be the highest when the surrounding elements have the same orientation as the stimulus within the center RF (Knierim and Van Essen, 1992; Cavanaugh et al., 2002c; Self et al., 2014). Surround excitation is less commonly observed and has largely been reported in cases where the stimulus in the center RF is not salient, such as low contrast (Levitt and Lund, 1997; Polat et al., 1998; Keller et al., 2020b).

In general, contextual modulation of visual responses depends on a variety of stimulus features such as contrast and

size of the grating presented in the RF center (Levitt and Lund, 1997; Kapadia et al., 1999; Sceniak et al., 1999; Polat et al., 1998; Cavanaugh et al., 2002b), the difference in orientation between center and surround stimuli (Knierim and Van Essen, 1992; Cavanaugh et al., 2002c), and the spatial resolution of the surround pattern (Li et al., 2006). Although these stimulus features interact with each other (Kapadia et al., 1999), they are usually studied independently due to limited experimental time. Moreover, parametric stimuli such as gratings likely drive visual neurons sub-optimally. This is because many visual neurons — like in mouse V1 (Walker et al., 2019; Franke et al., 2022; Ustyuzhaninov et al., 2022) and primate higher visual areas (Pasupathy and Connor, 2001; Bashivan et al., 2019) — exhibit strong selectivity to complex stimuli like corners, checkerboards or textures.

The dependence of contextual modulation on different stimulus features and the strong neuronal preference for complex visual stimuli calls for a more systematic and data-driven way to characterize center-surround interactions using stimuli with ecologically relevant statistics. So far, this has been challenging due to the high dimensionality of natural stimuli and the difficulty in interpreting neuronal responses to a natural input. Here, we overcome these challenges and systematically study center-surround modulations in mouse V1 using naturalistic stimuli by performing inception loops, a closed-loop paradigm circling between large-scale neuronal recordings, convolutional neural network (CNN) models that accurately predict neuronal responses to arbitrary natural stimuli, *in silico* optimization of non-parametric center and surround images and *in vivo* verification (Walker et al., 2019; Franke et al., 2022; Bashivan et al., 2019).

Using our data-driven CNN model, we synthesized non-parametric surround images that maximally excite and inhibit the activity of mouse V1 neurons to their optimal visual stimulus in the RF center and subsequently verified their accuracy *in vivo*. Synthesized surround images contained complex features also present in natural scenes, but were more effective in modulating neuronal activity than natural surround images. Interestingly, we found that the excitatory surround stimuli appeared congruent, completing the spatial pattern of the center stimulus, whereas the inhibiting surround stimuli appeared incongruent. We confirmed this qualitative effect by showing that when we extrapolated the natural image statistics of the center into the surround, the resulting surround images resembled model-derived optimized excitatory surrounds. In addition, excitatory surround images, compared to inhibitory ones, exhibited a larger similarity in neuronal response space to natural scenes, which are known to be spatially correlated and congruent (Geisler et al., 2001; Sigman et al., 2001). Finally, we showed that excitation and inhibition of visual activity by congruent and incongruent surround stimuli, respectively, emerge within a simple hierarchical generative model that encodes an important aspect of natural scene statistics, which is long-range spatial correlations, thereby supporting a new functional role of contextual modulation in sensory processing. Our results regarding contextual modulation are reproduced in a large-scale functional

connectomics dataset spanning multiple areas of mouse visual cortex (MICrONS Consortium et al., 2021), which opens the way to dissect its circuit mechanism, including delineating the role of lateral and feedback recurrent connections.

Our work is the first data-driven approach to study contextual interactions in the mouse visual system. It can be easily adapted to other visual areas, animal species and sensory systems, providing the unique possibility to systematically study how context shapes neuronal tuning.

## Results

### Deep neural network model accurately predicts center-surround modulation of visual responses in mouse primary visual cortex

We combined large-scale population imaging and neural predictive modeling to systematically characterize contextual modulation in mouse primary visual cortex (V1). The experimental and modeling setup was adapted based on (Walker et al., 2019). Specifically, we used two-photon imaging to record the population calcium activity in L2/3 of V1 (630x630  $\mu\text{m}$ , 10 planes, 7.97 volumes/s) in awake, head-fixed mice positioned on a treadmill, while presenting the animal with natural images (Fig. 1a,b). To capture center-surround interactions, we presented full-field natural images, which activate both center (classical RF) and surround (extra-classical RF) of V1 neurons, and local masked images that predominantly drive the center of the recorded neurons. Natural images were masked by applying an aperture of  $48^\circ$  visual angle in diameter in the center of the image. For each functional recording, the center RF across all recorded neurons – estimated as minimal response field (MRF) using a sparse noise stimulus (Jones and Palmer, 1987) – was centered on the monitor (Fig. 1c). This ensured that the RF center of the majority of neurons was within the area of the presented masked images. Then, we used the recorded neuronal activity in response to full-field and masked natural images to train a convolutional neural network (CNN) model to predict neuronal responses as a function of visual input. The model also considered eye movements and the modulatory gain effect of the animal's behavior on neuronal responses (Niell and Stryker, 2010), by using the recorded pupil and running speed traces as input to a shifter and modulator network (Fig. 1d; Walker et al., 2019). An example model (architecture shown in Fig. 1e) that was trained on 7,741 neurons and 4,182 trials (i.e. images) yielded a normalized correlation between model predictions and mean observed responses of  $0.73 \pm 0.20$  (mean  $\pm$  standard deviation; Fig. 1f). This is comparable to state-of-the-art models of mouse V1 (Franke et al., 2022; Willeke et al., 2022; Lurz et al., 2021). Importantly, masking half of the training images improved the model's prediction of contextual modulation (Fig. 1g): The prediction of how neuronal responses differ between a masked image and its full-field counterpart significantly increased when using masked natural images during model training (for statistics, see figure legend). Together, this shows that our deep neural network approach accurately captures center-surround modulation of visual responses in mouse primary visual cortex, allowing us to study contextual

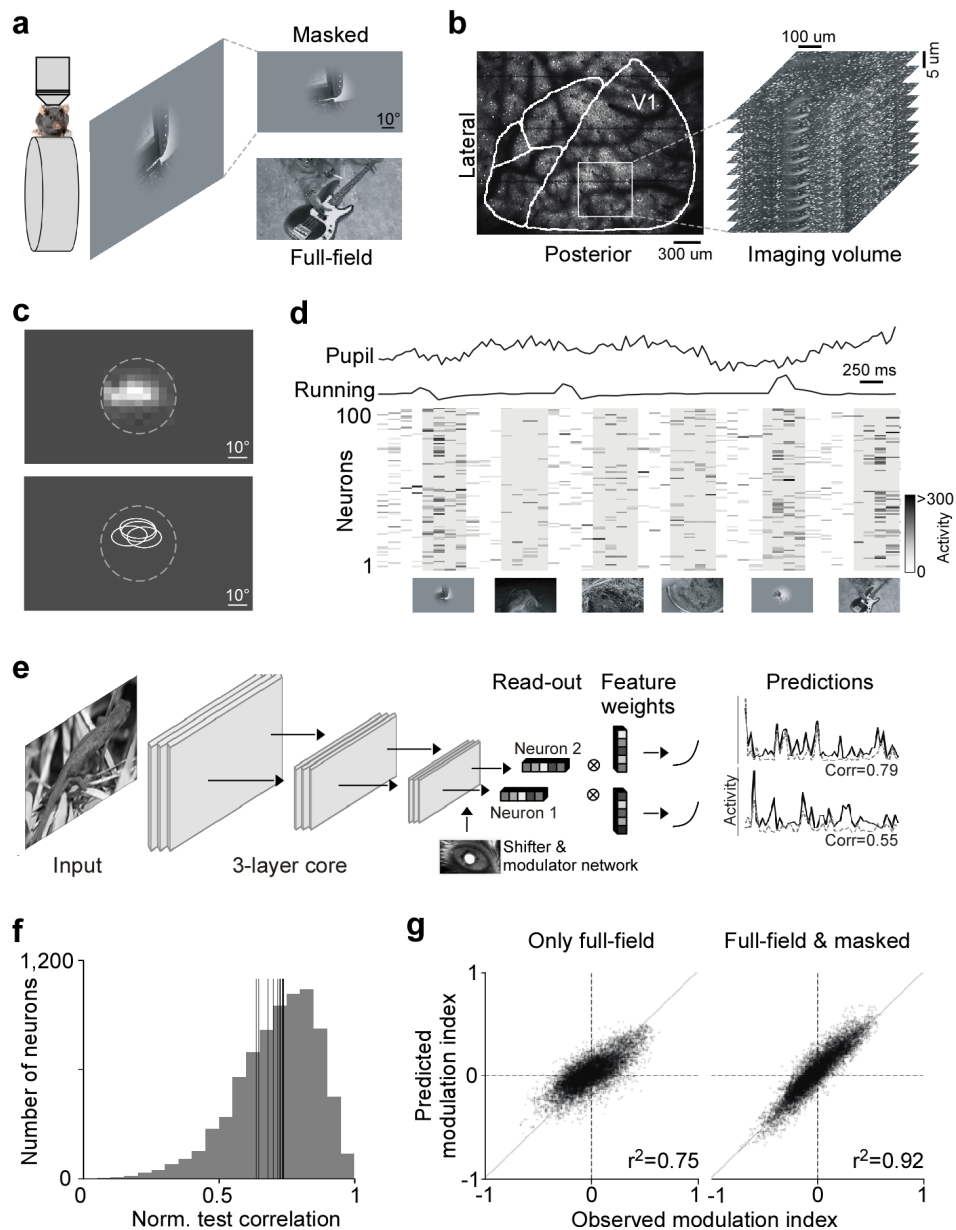


**Fig. 1. Deep neural network approach captures center-surround modulation of visual responses in mouse primary visual cortex.** **a**, Schematic of experimental setup: Awake, head-fixed mice on a treadmill were presented with full-field and masked natural images from the ImageNet database, while recording the population calcium activity in V1 using two-photon imaging. **b**, Example recording field. GCaMP6s expression through cranial window, with the borders of different visual areas indicated in white. Area borders were identified based on the gradient in the retinotopy (Garrett et al., 2014). The recording site was chosen to be in the center of V1, mostly activated by the center region of the monitor. The right depicts a stack of imaging fields across V1 depths (10 fields, 5 $\mu$ step in z, 630x630 $\mu$ , 7.97 volumes/s). **c**, Top shows heat map of aggregated population RF of one experiment, obtained using a sparse noise stimulus. The dotted line indicates the aperture of masked natural images. The bottom shows RF contour plots of n=4 experiments and mice. **d**, Raster plot of neuronal responses of 100 example cells to natural images across 6 trials. Trial condition (full-field vs. masked) indicated below each trial. Each image was presented for 0.5s, indicated by the shaded blocks. **e**, Schematic of model architecture. The network consists of a convolutional core, a readout, a shifter network accounting for eye movements by predicting a gaze shift, and a modulator predicting a gain attributed to behavior state of the animal. Model performance was evaluated by comparing predicted responses to a held-out test set to observed responses. **f**, Distribution of normalized correlation between predicted and observed responses averaged over repeats (maximal predictable variability) for an example model trained on data from n=7,741 neurons and n=4,182 trials. Vertical lines indicate mean performance of other animals. **g**, Accuracy of model predictions of surround modulation for only full-field versus full-field and masked natural images. Each test image was presented in both full-field and masked, allowing us to compute a surround modulation index per image per neuron. The modulation indices across images were averaged per neuron. Left and right shows predicted vs. observed surround modulation indices for a model trained on only full-field images and full-field and masked images, respectively. The model trained on both full-field and cropped images predicted surround modulation significantly better than the model trained on only full-field images (p-value<0.001). The total number of training images was the same, and the data was collected from the same animal in the same session.

modulation in the setting of complex and naturalistic visual stimuli.

**CNN model identifies non-parametric excitatory and inhibitory surround images of mouse V1 neurons** We used the trained CNN model as a “digital twin” of the mouse vi-

ual cortex to identify non-parametric surround images that greatly modulate neuronal activity. For that, we focused on the most exciting and most inhibiting surround image, which enhances and reduces the response of a single neuron to its optimal stimulus in the center, respectively. The rationale

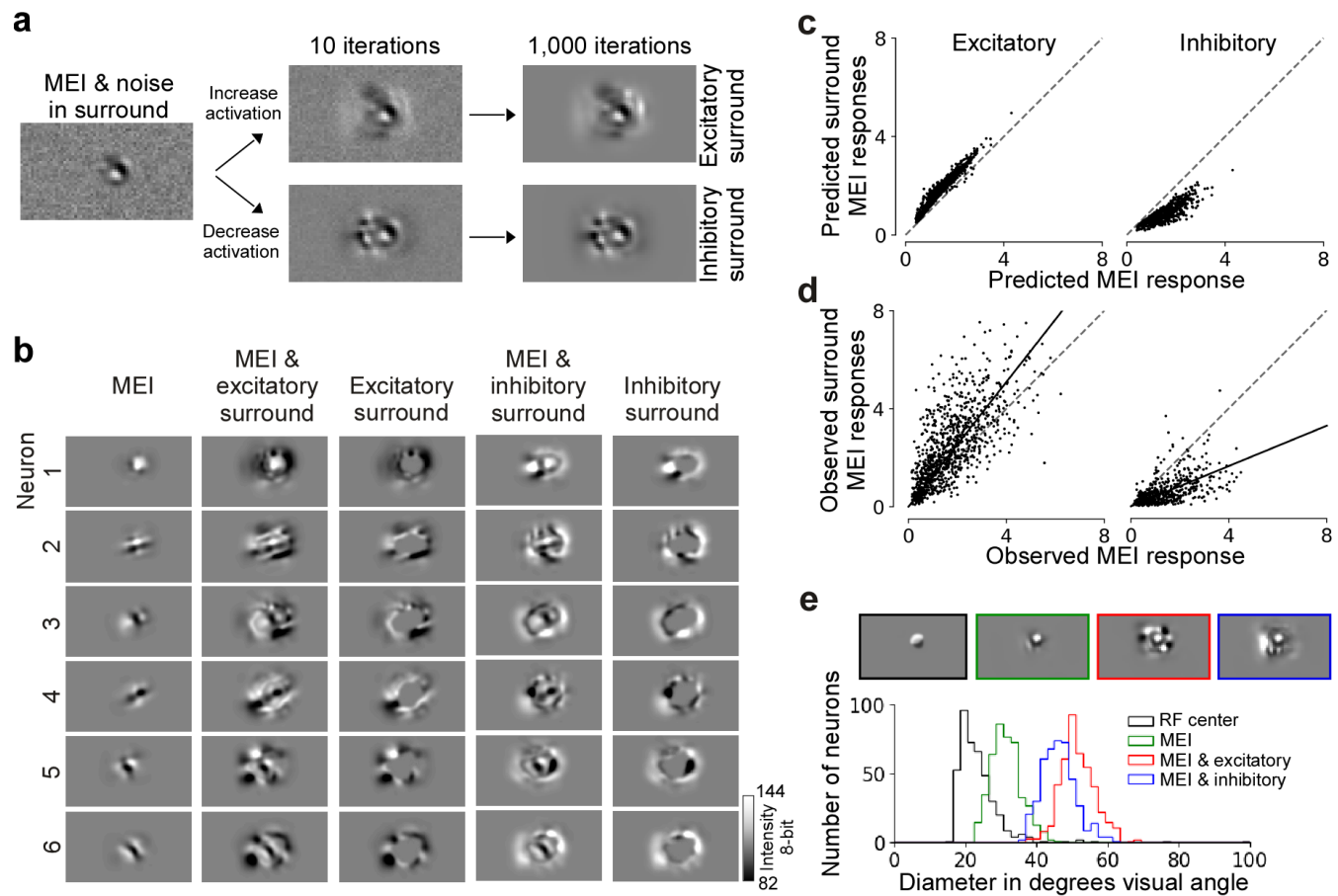


**Fig. 2. Modeling approach accurately predicts non-parametric excitatory and inhibitory surround images of single neurons in mouse V1.** **a**, Schematic of the optimization of surround images. The initial image is Gaussian noise with the center replaced by the MEI. During optimization, the gradient only flows in the region where the inverse MEI mask is non-zero, leaving the center unchanged. We optimized for the most exciting or the most inhibiting image in the surround. After 1,000 iterations, we reached the final image of the excitatory or the inhibitory surround. **b**, Panel shows MEI, excitatory surround with MEI, the difference between the two, inhibitory surround with MEI, and the difference between the two for 5 example neurons. Since the gradient was set to zero during optimization for the area within the MEI mask, the center remained the same as the MEI. **c**, Model predicted responses to the excitatory (left) and inhibitory (right) surround images (y-axis), compared to the predicted responses to the MEIs (x-axis). Responses are depicted in arbitrary units, corresponding to the output of the model. **d**, Observed responses to the excitatory (left) and inhibitory (right) surround (y-axis), compared to the observed responses to the MEIs (x-axis). For each neuron, responses are normalized by the standard deviation of responses to all images. Across the population, the modulation was significant for both excitatory (p-value= $1.15 \times 10^{-75}$ , Wilcoxon signed rank test) and inhibitory surround images (p-value= $8.79 \times 10^{-71}$ ). Across stimulus repetitions, 28.4% neurons responded significantly stronger to the excitatory surround image than to the MEI (n=6 animals, 960 cells, two-sided t-test, p-value<0.05) while 2.6% responded weaker. 55.1% neurons responded significantly weaker to the inhibitory surround image than to the MEI while 0.4% responded stronger (n=3 animals, 510 cells). Solid line indicates the regression line across the population, and dotted gray line indicates the diagonal. **e**, Diameters of RFs estimated using sparse noise, the MEIs, and the MEIs with excitatory and inhibitory surround. The mean of center RF (gray distribution) sizes across all neurons (n=4, 419 cells) is  $23.4 \text{ degrees} \pm 0.34$  (mean  $\pm$  s.e.m.). The mean of the MEI (green distribution) size across all neurons (n=4, 434 cells) is  $31.3 \text{ degrees} \pm 0.20$ . The size of the MEI is larger than the center RF. The sizes of both the excitatory (red distribution) and inhibitory (blue distribution) surround are much larger than the center RF, measuring  $51.4 \pm 0.23$  and  $46.1 \pm 0.23$  (mean  $\pm$  s.e.m.) respectively (n=4, 434 cells).

behind this approach was to identify surround images that maximally modulate the encoding of the neuron's preferred visual feature. To identify the optimal center stimulus per neuron, we first optimized the most exciting input (MEI) using gradient ascent as previously described (Walker et al., 2019; Franke et al., 2022). In the following, we use the MEI as approximation for the RF center and consider all visual space beyond the MEI as RF surround. To generate excitatory and inhibitory surround images, we used a second optimization step that started with the MEI and initial Gaussian noise in the surround and during optimization, only pixels in the surrounding area of the MEI were updated (Fig. 2a). Thereby, the center (i.e. MEI) of the surround images remained unchanged while redistributing the contrast in the surround (Suppl. Fig. 1a and b). This yielded complex surround images of V1 neurons (Fig. 2b), which were predicted

by the model to either enhance or reduce visual responses to optimal stimuli in the center (Fig. 2c). Interestingly, the excitatory surround images were predicted to be less effective in modulating the neurons' activity than the inhibitory ones (Fig. 2c).

To verify the efficacy of the synthesized surround images *in vivo*, we performed inception loop experiments (Walker et al., 2019; Bashivan et al., 2019): After model training and stimulus optimization, we presented MEIs and the respective surrounds back to the same mouse on the next day while recording from the same neurons, thereby testing whether they effectively modulate neuronal responses as predicted by the model. We found that the *in silico* predictions (Fig. 2c) matched the *in vivo* results (Fig. 2d, Suppl. Fig. 2): The responses of the neuronal population significantly increased and decreased by the synthesized excitatory and inhibitory

surround images, respectively, compared to presenting the MEI alone. While 55.1% of the neurons verified *in vivo* during inception loop experiments were significantly inhibited by their inhibitory surround images across stimulus repetitions, only 28.4% were significantly facilitated by their excitatory surround images, in line with the lower modulation strength of excitatory compared to inhibitory surround images predicted by the model. Critically, less than 3% were significantly modulated in the direction opposite to what the model predicted. These results from the inception loop experiments demonstrate the accuracy of our CNN model in predicting non-parametric modulatory surround images of mouse V1 neurons. Notably, we also reproduced the described center-surround effects in the large-scale multi-area functional connectomics MICrONS dataset (MICrONS Consortium et al., 2021) that used natural movies instead of static images as visual stimuli (Suppl. Fig. 3). This opens the way to dissect circuit mechanisms underlying contextual modulation in mouse visual cortex, including delineating the role of lateral and feedback recurrent connections.

We verified that the observed response modulations indeed originated from activating the surround (i.e. extra-classical RF) of the neurons. First, we demonstrated that the synthesized surround images extend beyond the center (i.e. classical RF) of the neurons (Fig. 2e). Specifically, we estimated each neuron's center RF as the minimal response field (MRF) using a sparse noise stimulus (Jones and Palmer, 1987) and compared its size to the size of the MEI and the excitatory and inhibitory surround, respectively. The MRF was, on average, smaller than the MEI, suggesting that the MEI itself corresponds to an overestimation of the RF center. Importantly, both the excitatory and inhibitory surround were much larger than the MRF, indicating that the modulatory effect on neuronal activity we observed by the surround images was indeed elicited by activating the surround component of V1 RFs. In line with this, in additional control experiments we show that the response modulation persisted *in silico* and *in vivo* in a "far" surround region not directly adjacent to the MEI (Suppl. Fig. 4). In addition, we showed that increasing the contrast in the center was more effective in driving the neurons than adding the same amount of contrast in the surround of the image (Suppl. Fig. 5), consistent with the idea that the enhancement in neuronal response from the surround is modulatory (Allman et al., 1985; Cavanaugh et al., 2002a; Jones et al., 2001; Knierim and Van Essen, 1992). Together, these results demonstrate that the observed response modulation by model-derived surround images originates from activating the surround RF of V1 neurons.

**Surround images are ecologically relevant and correspond to the optimal modulating stimulus** We next asked the question whether the center-surround modulation we observed with our non-parametric images exhibits ecological relevance, meaning that a similar contextual modulation of V1 neuronal activity can be observed with surround images present in ecological images. To address this, we compared the modulation elicited by model-derived surround images to the modulation by natural images. We focused this analy-

sis on natural image surrounds that contain the neuron's preferred center feature, similar to the optimized surround images that have the MEI in the center. To obtain surrounds of natural images, we therefore screened a new set of 5,000 masked natural images and identified the most exciting natural images per neuron (>80 % activation compared to the MEI activation), matching the size, location and contrast of its MEI (Fig. 3a). We then replaced the center of these images by the MEI, and masked the images to match the average size and contrast of excitatory and inhibitory surround images. For each neuron, this yielded a set of images with the same optimal stimulus in the center (i.e. the MEI), but diverse natural surrounds. To obtain the modulation strength of these natural surrounds, we presented the natural surround images to the model and compared the predicted activations to the activation of the MEI alone.

We found that there are indeed natural surrounds that enhance and reduce V1 model responses to the preferred visual feature, similar to our synthesized surround images (Fig. 3b). We tested this *in silico* prediction by performing inception loop experiments with the synthesized surround images and the most and least activating natural surrounds per neuron, as predicted by the model. Across the neuronal population, the most activating natural surrounds significantly enhanced V1 responses to their optimal center stimulus, while the least activating natural surround resulted in reduced activity (Fig. 3c). In addition, across the population, the synthesized inhibitory surround images were more effective in modulating V1 neuronal activity than the least activating natural surrounds (Fig. 3d). In contrast, the modulation strength of the most activating natural surround images was comparable to the synthesized excitatory surrounds (Fig. 3d). Together, these findings strongly suggest that the model-derived surround images exhibit ecological relevance, as they modulate V1 responses to their preferred center feature in a similar way as surround patches of natural images.

**Completion and disruption of center features characterize excitatory and inhibitory surround images** Center-surround modulation of visual activity corresponds to a neuronal implementation for integrating visual information across space, thereby providing context for visual processing. So far, little is known about the natural image statistics that drive contextual modulation in vision, due to the lack of tools that allow unbiased and systematic testing of such high-dimensional visual inputs. Here, we used our data-driven model and the optimized surround images to systematically investigate the rules that determine contextual excitation versus inhibition in a naturalistic setting.

We observed that the excitatory surround images appeared more congruent with respect to the MEI in the center compared to the inhibitory surround images (Fig. 4a). Spatial patterns in the MEI, such as orientation, were mostly maintained and completed by the excitatory surround but often disrupted and opposed by the inhibitory surround. Therefore, we hypothesized that the excitatory and inhibitory surround can be characterized by pattern completion and disruption, respectively, with respect to the preferred feature in the cen-

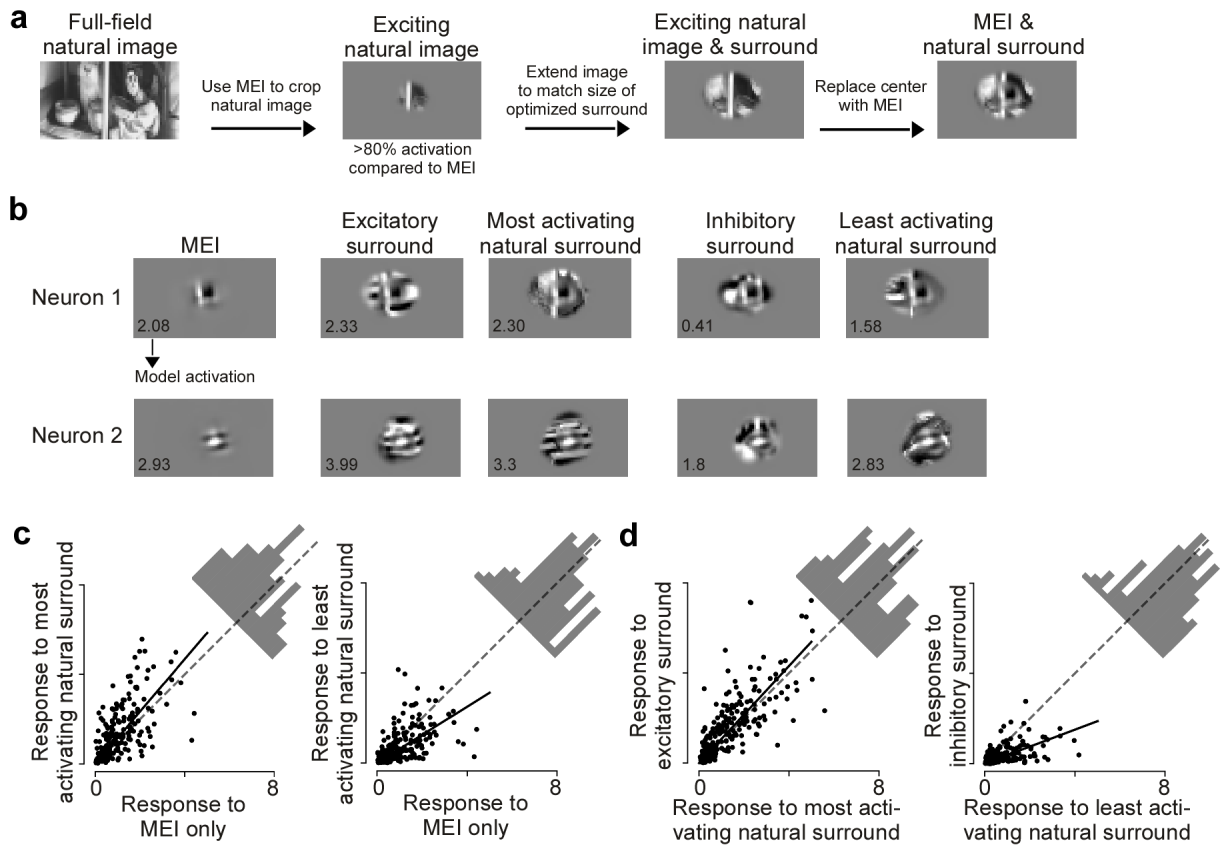


**Fig. 3. Surround images correspond to the optimal modulating stimulus and are ecologically relevant.** **a**, Schematic illustrating how we obtained natural surround images for one example neuron. **b**, Optimized excitatory and inhibitory surround images, most exciting and inhibiting natural surrounds and MEI of two example neurons. The predicted activation score is indicated in the bottom left of the images. **c**, Observed responses to the MEI with natural surround images compared to the MEI alone. Across the population, the least activating natural surround images suppressed neuronal response ( $p\text{-value}=1.84 \times 10^{-8}$ , Wilcoxon signed rank test), and the most activating natural surround images enhanced neuronal response ( $p\text{-value}=2.44 \times 10^{-9}$ , Wilcoxon signed rank test). Across stimulus repetitions, 23% responded significantly stronger to the most activating natural images than to the MEI ( $n=3$  animals, 226 cells, two-sided t-test,  $p\text{-value}<0.05$ ) and 25% of the neurons responded significantly weaker to the least activating natural surround images than to the MEI. Solid line indicates the regression line across the population, and dotted gray line indicates the diagonal. **d**, Observed responses to the MEI with natural surround images compared to the MEI with excitatory/inhibitory surround. Across the population, the MEI with inhibitory surround suppressed neuronal response more than the MEI with the least activating natural surround ( $p\text{-value}=1.98 \times 10^{-20}$ , Wilcoxon signed rank test). The MEI with excitatory surround enhanced neuronal response more than the MEI with most activating natural surround ( $p\text{-value}=1.05 \times 10^{-6}$ , Wilcoxon signed rank test). Across stimulus repetitions, 37% of neurons responded significantly weaker to the MEI with inhibitory surround compared to the MEI with the least activating natural surround and 19% of the neurons responded significantly stronger to the MEI with excitatory surround compared to the MEI with the most activating natural surround ( $n=3$  animals, 226 cells, two-sided t-test,  $p\text{-value}<0.05$ ). Solid line indicates the regression line across the population, and dotted gray line indicates the diagonal.

ter. We tested these predictions by performing a set of *in silico* experiments. First, we used the MEI in the RF center to extrapolate its spatial patterns into the surround based on a bivariate spline approximation, thereby creating a congruent surround that completes patterns present in the center (Fig. 4b). For most neurons, the extrapolated surround perceptually looked more similar to the excitatory than the inhibitory surround (Suppl. Fig. 6). To quantify the perceptual similarity of optimized and extrapolated surrounds, we computed the "representational similarity" for a given pair of images in the neuronal response space. We chose to use representational similarity instead of pixel-wise correlation to quantify similarity between images because (i) the representational space more closely mimics perceptual similarity (Kriegeskorte et al., 2008) and (ii) this process gets rid of irrelevant image features, such as high spatial frequency noise. Specifically, we presented the optimized and extrapolated surround images to the trained CNN model, obtained a vector of neuronal responses per image and estimated the cosine similarity between the response vectors of an image pair (i.e. extrapo-

lated and excitatory surround; Fig. 4b). We found that the extrapolated surround images that complete the spatial structure of the MEI exhibit a high representational similarity to the MEI with excitatory surround images, while the similarity to the MEI with inhibitory surrounds was much weaker (Fig. 4c). This suggests that excitatory surround images of V1 neurons are characterized by pattern completion of the optimal center stimulus.

We further tested this hypothesis by quantifying the statistics of our model-derived surround images. Specifically, we took advantage of the well-described fact that natural images are correlated across space and often contain congruent structures that form object contours and continuous patterns (Geisler et al., 2001; Sigman et al., 2001). Therefore, excitatory surround images should share statistical properties with and be perceptually similar to the surrounds of natural image patches, more so than inhibitory surround images. We compared the spatial correlation structure of optimized MEI with surround images to the one of natural surrounds that contain the neuron's preferred image feature in the center (>80% ac-

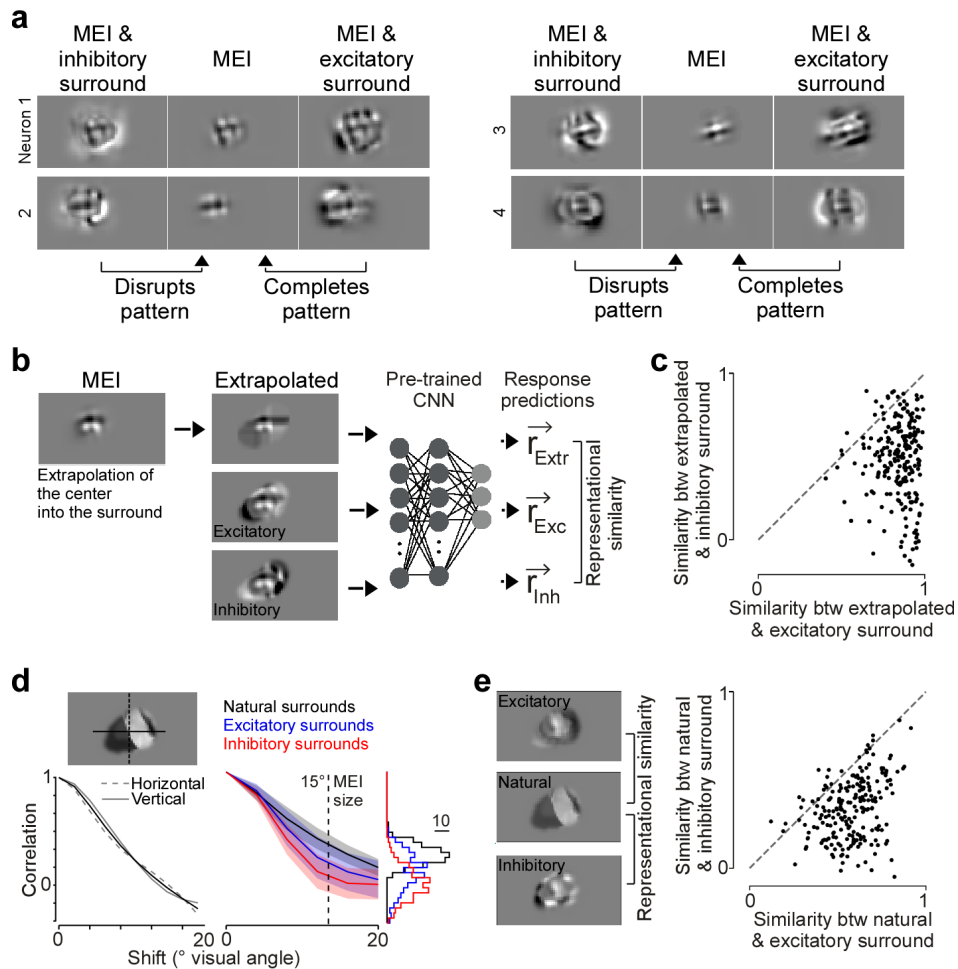


**Fig. 4. Pattern completion and disruption characterize excitatory and inhibitory surround images.** **a**, MEI with excitatory and inhibitory surround of four example neurons, illustrating that excitatory and inhibitory surround images complete and disrupt, respectively, spatial patterns of the MEI. **b**, MEI of example neuron, with extrapolated and excitatory and inhibitory surround images. Right shows a schematic illustrating how we compared the similarity of surround images using representational similarity. In brief, each surround image was presented to the trained CNN model to obtain a response vector. The response vectors for different images were then compared using Pearson's correlation coefficient. **c**, Representational similarity (as Pearson's correlation coefficient) of extrapolated surround images to excitatory and inhibitory surround ( $p$ -value= $2.26 \times 10^{-36}$ , two-sided Wilcoxon signed rank test,  $n=3$  animals, 219 neurons). **d**, Left shows auto-correlation function of an example natural surround image, for a vertical (dotted line) and horizontal (solid line) projection through the center of mass of the image (mean in black). Right shows the mean auto-correlation functions of natural (black), excitatory (blue) and inhibitory (red) surround images ( $n=3$  animals, 219 neurons; shading: s.d.), with the histograms of correlation coefficients for a spatial shift of  $15^\circ$  visual angle indicated on the right. For a shift of  $15^\circ$  visual angle, corresponding to the mean radius of MEIs, inhibitory surround images exhibited significantly weaker spatial correlations than excitatory surround images ( $p$ -value= $1.8 \times 10^{-15}$ , two-sided Wilcoxon signed rank test). **e**, Excitatory and inhibitory surround of an example neuron, with one exciting natural image and surround (left) and representational similarity (as Pearson's correlation coefficient, right;  $p$ -value= $5.28 \times 10^{-35}$ , two-sided Wilcoxon signed rank test,  $n=3$  animals, 219 neurons) of natural surround images with excitatory and inhibitory surround. Each dot represents the mean across natural surrounds per neuron.

tivation compared to the MEI activation). Spatial correlations were quantified using the auto-correlation function of intensity profiles through the center of the surround images (Fig. 4d). We found that, like natural image patches, the MEI with excitatory surround displayed significantly higher spatial correlations than the MEI with the inhibitory surround image (Fig. 4d), at least for spatial shifts of the mean MEI size across neurons. Next, we used the representational similarity metric introduced above to quantify the similarity between optimized and natural center-surround images. This revealed that natural surround images with the neuron's preferred center feature exhibit a larger similarity with excitatory than inhibitory surround images (Fig. 4e). Taken together, our results demonstrate that surround excitation and inhibition in mouse primary visual cortex can be characterized by pattern completion and disruption, respectively, thereby identifying a clear relationship between natural image statistics and mod-

ulation of neuronal activity.

#### Probabilistic perception via Bayesian inference can explain observed center-surround effects

Finally, we linked our observed center-surround effects to normative, first-principle theories of perceptual inference. In general, the goal of perception is to infer useful features from the world, but given that ambiguous, noisy sensory stimuli often conceal these features, it is beneficial to combine information from the incoming sensory stimulus with prior knowledge of the environment (Von Helmholtz, 1867). One principled way how the brain could accomplish this is to perform Bayesian inference over relevant latent variables (features) underlying the stimulus using a statistical generative model of the world (Knill and Richards, 1996; Kersten et al., 2004; Lochmann and Denève, 2011; Fiser et al., 2010). Here, we demonstrate that surround excitation and inhibition by congruent and incongruent

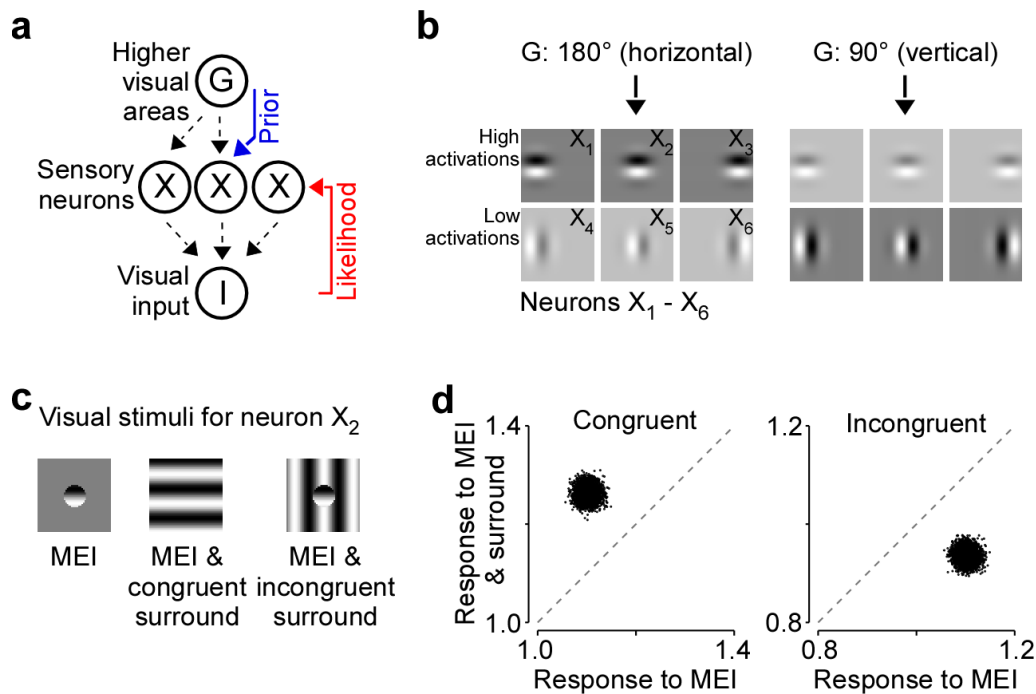


**Fig. 5. Explaining observed center-surround effects via Bayesian inference and neural sampling.** **a**, Assumed hierarchical generative model of the stimulus as maintained by the brain.  $G$  represents a higher visual area, encoding a global orientation variable,  $X$  represents sensory neuronal responses, which are activations of local Gabor filters, and  $I$  represents the visual input. The idea is that when visual input  $I$  is presented, the (simplified model of the) brain probabilistically infers a global orientation and the activations of the Gabor filters from the visual input via posterior inference, i.e., computes  $p(G, X|I)$  and samples from it. Posterior samples of  $X$ , i.e., of sensory neurons depend on the visual input  $I$  (likelihood, feedforward) as well as on  $G$  (prior, feedback). **b**, Gabor filters corresponding to the 6 model neurons as activated only by the prior, i.e., by  $G$ . In our model, we have 3 neurons with vertical Gabor filters and 3 others with horizontal Gabor filters. Gabor filters that have orientations similar to the global orientations have higher activations, as opposed to those that have orientations dissimilar to the global orientation. These activations are interpreted as sensory neuronal responses. We consider the neuron with a horizontal Gabor at the center as the "center neuron". **c**, Collection of visual stimuli we present to the model. All stimuli, i.e., MEI, MEI & congruent surround, and MEI & incongruent surround are defined w.r.t the center neuron. **d-f**, Scatterplot of posterior samples from the center neuron under various stimulus presentations, reproducing the key experimental observations of surround-based excitation and inhibition.

surround patterns, respectively, is consistent with this theory by using a simple hierarchical generative model of the stimulus that encodes long-range spatial correlations of natural image statistics in its prior.

Our hierarchical generative model is similar to ones previously proposed (Haefner et al., 2016; Bányai et al., 2019). Specifically, in our model we assume that a set of oriented Gabor-shaped filters located in the center and surround of visual space are linearly combined to generate the observed image  $I$  (Fig. 5a). We further assume that the activation of each of these filters depends on a global orientation variable,  $G$ , which boosts the activity of compatible filters, and suppresses those of incompatible filters (Fig. 5b). Upon observing a stimulus, i.e. during perception, the brain inverts the generative model to compute the posterior distribution  $p(G, X|I)$ . Specifically, the brain combines the latent global orientation  $G$  which is provided by feedback from higher areas and the feedforward sensory information given the image  $I$ . As a result of this inference process, the neuronal responses  $X$  to a given stimulus are influenced by both the stimulus  $I$  and the global orientation  $G$ .

To quantify the center-surround interactions in this model, we presented three stimuli tailored to an example sensory neuron whose RF is located in the center of visual space (Fig. 5c): (1) the MEI of the example neuron, (2) the MEI with a spatially congruent stimulus in the surround, (3) the MEI with a spatially incongruent stimulus in the surround. These three

conditions match the pattern completion and disruption that characterize the contextual modulations we found in mouse V1. For each stimulus condition, we computed the posterior  $p(G, X|I)$  in our hierarchical model to obtain a distribution of global orientations and responses given the stimulus condition. The model responses reproduced our key experimental results (Fig. 5d): (1) the example neuron is driven strongly by the MEI alone, (2) the spatially congruent stimulus drives the example neuron in the center stronger than its MEI, (3) the spatially incongruent stimulus inhibits the responses of the neuron, despite the MEI being present in the center.

In summary, our probabilistic inference model reproduced the main experimental findings of our study, with congruent surround stimuli being excitatory and incongruent surround stimuli being inhibitory with respect to the neuron's preferred feature. The key driver of this behavior in our model is the higher certainty about the global orientation induced by congruency of center and surround and, as a result, a stronger prior on the lower level features of similar orientation. As a result, even neurons with RFs in the center are more strongly activated.

## Discussion

Our study discovered a novel rule of surround modulation in mouse V1: Completion (or extension) of visual features in the RF center governed surround excitation, whereas disrupt-



tion (or termination) of RF center features produced inhibition. Non-linearity and high dimensionality in the neuronal responses to natural images have so far made it challenging to accurately define the RF center properties and to model the interactions with the RF surround. Our accurate digital twin models allowed us to model the non-linearity both within and beyond the RF center, and to predict the best modulating stimuli in the surround without any parametric assumptions about their underlying statistical structure. We verified the predictions from the model experimentally in a closed-loop manner, and found that combining an optimal stimulus in the RF center with an excitatory surround yielded images that were more similar to natural scenes than images consisting of optimal center stimulus and inhibitory surround. This type of surround facilitation by congruent structures emerged within a simple hierarchical model that modulates neuronal responses based on prior knowledge of natural scene statistics, and may potentially enhance the encoding of prominent features in the visual scene, such as contours and edges, especially when the sensory input is noisy and ambiguous.

**Relationship between surround modulation and stimulus statistics** Classical studies in monkeys have investigated the spatial patterns driving contextual modulation in primary visual cortex using oriented stimuli such as gratings and bars (Knierim and Van Essen, 1992; Levitt and Lund, 1997; Kapadia et al., 1999; Sceniak et al., 1999; Cavanaugh et al., 2002b,c; Nassi et al., 2013; Nurminen et al., 2018). This revealed that suppression is the dominant form of surround modulation and that surround stimuli congruent with the center stimulus tend to be the most suppressive (Knierim and Van Essen, 1992; Levitt and Lund, 1997; Kapadia et al., 1999; Sceniak et al., 1999; Cavanaugh et al., 2002b,c; Nassi et al., 2013; Nurminen et al., 2018). The suppression strength decreased as the surrounding stimulus becomes less congruent (Knierim and Van Essen, 1992; Kapadia et al., 1999). In contrast, surround facilitation has been much more rarely observed, and it requires more specific configurations of the center stimulus such as low contrast or even absence of stimulation (Polat et al., 1998; Lee and Nguyen, 2001). This is in line with our finding that excitatory surround images are less effective in modulating visual responses than inhibitory surround images.

However, our results based on naturalistic stimuli and a data-driven approach, which does not make any assumptions about stimulus selectivity, reveal a different principle of surround modulation in mouse primary visual cortex. We find that the most excitatory surround stimulus is congruent with respect to the center stimulus, while the most inhibiting surround stimulus is incongruent. So far, the spatial patterns driving surround excitation versus inhibition in mouse V1 are less conclusive compared to primates. Some previous studies have reported suppression and facilitation of mouse V1 neurons by congruent and incongruent parametric surround stimuli (Keller et al., 2020a; Self et al., 2014), respectively, consistent with the results in primates. However, there seems to be a large variability across neurons, where surround stimuli that have the same orientation as the center stimulus can

be either excitatory or inhibitory (Samonds et al., 2017) and different orientations of the surround relative to the center can be excitatory (Keller et al., 2020b). In part, this variability across neurons might be related to the fact that parametric stimuli like gratings and bars drive mouse V1 neurons sub-optimally, due to the neurons' selectivity for more complex visual features (Walker et al., 2019). It is well established that contextual modulation depends on the center stimulus (Knierim and Van Essen, 1992; Kapadia et al., 1999) and, therefore, it might be critical to condition surround stimuli on the optimal stimulus in the RF center, corresponding to the MEI (Walker et al., 2019).

The inconsistencies in surround patterns eliciting excitation and inhibition reported in studies on mouse and primate V1 might partially be due to differences in stimulus design. For example, the complex naturalistic stimuli we used vary from parametric stimuli with respect to image statistics and likely result in different neuronal responses (Froudarakis et al., 2014; David et al., 2004), which may influence the modulatory effect of the surround on the RF center. Other critical stimulus parameters that impact neuronal responses are stimulus contrast and luminance. It has been previously shown that at lower contrast, congruent surround stimuli facilitate responses in monkey V1 neurons to the preferred center stimulus (Polat et al., 1998), similar to the pattern of surround excitation we describe here. In monkeys, surround facilitation turned into suppression as the contrast of the center stimulus increased (Polat et al., 1998). We optimized the MEIs and surround images to minimize clipping of pixel values outside the 8-bit range, even for the contrast-matched MEIs that had higher contrast in the center (cf. Suppl Fig. 4), and presented them at mesopic light levels. Without further experiments, it is challenging to compare our non-parametric MEIs and surround stimuli to previous results using parametric grating stimuli presented at varying contrasts and light levels (Polat et al., 1998; Adesnik et al., 2012; Keller et al., 2020b,a). Importantly, it is worth noting that, in addition to the experimental and technical differences described above, there likely exist species-specific differences in the stimulus statistics that drive surround modulation. Primates and mice may have distinct strategies in visual processing due to ethological differences, and, therefore, surround modulation of visual responses might serve a different computational goal. Future experiments are required to further understand possible species-specific roles of contextual modulation in vision.

**Circuit-level mechanism of contextual modulation in visual cortex** Mechanistically, surround suppression in V1 can be partially accounted for by feedback projections from higher visual areas. In monkeys, inactivation of feedback from V2 and V3 reduces surround suppression induced by large grating stimuli (Nassi et al., 2013; Nurminen et al., 2018) and also results in an increase in RF size (Sceniak et al., 1999; Nurminen et al., 2018). In mice, feedback from higher visual areas also strongly modulates V1 responses to center stimuli and even elicits strong responses without any stimulation of the center RF, thereby creating a feedback RF (Keller et al., 2020b; Shen et al., 2022). The cellular substrate of surround

modulation has been predominantly studied in mice, due to available genetic tools for cell-type specific circuit manipulations. Different types of inhibitory neurons have been identified as key players of surround modulation, including somatostatin (SOM)- and vasoactive intestinal peptide (VIP)-expressing cells, which inhibit each other as well as excitatory V1 neurons and are further modulated by feedback (Adesnik et al., 2012; Keller et al., 2020a; Shen et al., 2022). Based on these results, surround suppression in mouse V1, and likely primate V1, is dependent on the exact balance between the excitatory input from feedforward and feedback projections and the inhibitory inputs from locally present inhibitory neuron types.

To further explain surround modulation of individual visual neurons as a function of local and long-range network connectivity, one can take advantage of recent advances in functional connectomics, combining large-scale neuronal recordings with detailed anatomical information at the scale of single synapses. Here, we demonstrated that the observed center-surround effects of mouse V1 neurons were reproduced in a recently published functional connectomics dataset (MICrons dataset) spanning V1 and multiple higher areas of mouse visual cortex (MICrONS Consortium et al., 2021). Specifically, this dataset includes responses of >75k neurons to natural movies and the reconstructed sub-cellular connectivity of the same cells from electron microscopy data. A dynamic recurrent neural network (RNN) model of this mouse's visual cortex exhibits not only a high predictive performance for natural movies, but also accurate out-of-domain performance on other stimulus classes such as drifting Gabor filters, directional pink noise, and random dot kinematograms (Wang et al., 2023). We took advantage of the model's ability to generalize to other visual stimulus domains and showed that MEIs and surround images optimized using the RNN model trained on the same natural movies used in the MICrons dataset closely resemble those obtained from our model. The MICrons dataset provides ample resources to link connectivity among neurons within V1 and across areas to the functional properties observed with regard to contextual modulation, thereby further delineating the role of local and feedback recurrent connections.

**Theoretical implications of surround facilitation** We discovered that surround facilitation is a prominent feature of contextual modulation in mouse primary visual cortex, thereby highlighting that center-surround interactions cannot simply be explained by suppression of sensory responses. Importantly, excitatory surround images with the optimal center stimulus exhibited a high representational similarity with natural images, indicating that congruent patterns frequently present in natural scenes (Geisler et al., 2001; Sigman et al., 2001) are associated with high neuronal activations. Excitation by congruent surround structures relative to the center may be explained by preferential long-range connections between neurons with co-linearly aligned RFs described in mice (Iacaruso et al., 2017) and higher mammals (Bosking et al., 1997; Schmidt et al., 1997; Sincich and Blasdel, 2001) and might serve perceptual phenomena like edge

detection, contour integration and object grouping observed in humans and primates (Kapadia et al., 1995; Geisler et al., 2001).

Our empirical results of surround facilitation are surprising in the light of a long line of theoretical work that explains sensory responses using principles like redundancy reduction (Barlow et al., 1967) or predictive coding (Rao and Ballard, 1999). The idea that neurons should minimize redundancy has given rise to contrast normalization models (Schwartz and Simoncelli, 2001) that were recently expanded to a flexibly-gated center-surround normalization model (Coen-Cagli et al., 2015) most relevant to our data. The key idea behind the latter model is to only normalize (typically reduce) center activation when the surround is similar, and otherwise ignore the surround. This proposal cannot explain our empirical findings. Analogously, predictive coding proposes that neuronal activity reflects prediction errors, and that therefore the center activation should be lower when it can be well predicted from the surround (Rao and Ballard, 1999; Keller and Mrsic-Flogel, 2018) – again in contradiction to our finding that excitatory surrounds appear to ‘complete’ the center stimulus, and frequently occurring in natural scenes.

In contrast, our results are expected within an alternative framework for understanding sensory neurons: perceptual (Bayesian) inference (Von Helmholtz, 1867; Knill and Richards, 1996). Here, sensory responses compute beliefs about latents in a hierarchical model with higher level latents both representing larger, more complex features of the image and acting as priors on lower level latents that represent localized parts of the image via feedback signals (Lee and Mumford, 2003). In such a model, global image structure can increase or decrease responses of neurons with localized RFs, depending on whether the global structure increases or decreases the probability of the local feature being present in the image (Haefner et al., 2016; Bányai et al., 2019). In fact, our toy-model which qualitatively reproduces our empirical findings is an example of such a model. Our approach of characterizing contextual modulation in a data-driven way for arbitrary stimuli, without any assumptions about neuronal selectivity, have revealed a novel relationship between surround modulation and natural image statistics, providing evidence for a role of contextual modulation in hierarchical inference, rather than only minimizing redundancy or prediction errors.

## Materials and Methods

**Animals and surgical preparation** All experimental procedures complied with guidelines of the NIH and were approved by the Baylor College of Medicine Institutional Animal Care and Use Committee (permit number: AN-4703), expressing GCaMP6s in cortical excitatory neurons. Mice used in this study (n=7, 3 males and 4 female, aged 2.5 to 3.5 month) were heterozygous crosses between Ai162 and Slc7a7-Cre transgenic lines (JAX #031562 and #023527, respectively). To expose V1 for optical imaging, we performed a craniotomy and installed a window that was 4mm in diameter and centered at 3mm lateral to midline and 2mm anterior to lambda (Reimer et al., 2014; Froudarakis et al., 2014).

Mice were housed in a facility with reverse light/dark cycle to ensure optimal alertness during the day when experiments were performed.

**Neurophysiological experiments and data processing** We recorded calcium signals using 2-photon imaging with a mesoscope (Sofroniew et al., 2016) which was equipped with a custom objective (0.6 numerical aperture, 21 mm focal length). The imaging fields of each recording were  $630 \times 630 \mu\text{m}^2$  per frame at 0.4 pixels  $\mu\text{m}^{-1}$  xy resolution and were positioned in the center of V1 according to the retinotopic map (Fig. 1b). Z resolution was 5  $\mu\text{m}$  with a total of ten planes from  $-200 \mu\text{m}$  to  $-245 \mu\text{m}$  relative to cortical surface. The laser power increased exponentially as imaging plane moved farther from the surface according to:

$$P = P_0 e^{z/L_z}$$

Here  $P$  is the laser power used at target depth  $z$ ,  $P_0$  is the power used at the surface ( $19.71 \text{ mW} \pm 4.68$ , mean  $\pm$  standard deviation), and  $L_z$  is the depth constant (220  $\mu\text{m}$ ). The highest laser output was of  $54.79 \text{ mW} \pm 13.67$  and was used at approximately 240  $\mu\text{m}$  from the surface. Most scans did not require more than 50 mW at maximal depth, except for one mouse where the average laser power at the deepest scanning field was 82.03 mW.

For each animal, we first performed retinotopic mapping across the whole cranial window to identify the border of V1 (Fig. 1b and c; Schuett et al., 2002). At the beginning of each imaging session, we measured the aggregated population RF to ensure precise placement of the monitor with regard to the imaging site. We used stimuli consisting of dark (pixel value=0) square dots of size 6 degrees in visual angle on a white background (pixel value=255). The dots were randomly displayed at locations on a 10 by 10 grid covering the central region of the monitor and at each location the dot was shown for 200 ms and repeated 10 times over the whole duration of dot mapping. The mean calcium signal was deconvolved and averaged across repeated trials to produce the population RF. The monitor was placed such that the population RF was centered on the monitor.

The full two-photon imaging processing pipeline is available at (<https://github.com/cajal/pipeline>). Briefly, raster correction for bidirectional scanning phase row misalignment was performed by iterative greedy search at increasing resolution for the raster phase resulting in the maximum cross-correlation between odd and even rows. Motion correction for global tissue movement was performed by shifting each frame in x and y to maximize the correlation between the cross-power spectra of a single scan frame and a template image, generated from the Gaussian-smoothed average of the Anscombe transform from the middle 2000 frames of the scan. Neurons were automatically segmented using constrained non-negative matrix factorization, then traces were deconvolved to extract estimates of spiking activity, within the CalmAn pipeline (Giovannucci et al., 2019). Cells were further selected by a classifier trained to separate somata versus artifacts based on segmented cell masks, resulting in exclusion of 8.1% of the masks.

A 3D stack of the volume imaged was collected at the end of each day to allow registration of the imaging plane and identification of unique neurons. The stack was composed of two volumes of 150 planes spanning from 50  $\mu\text{m}$  above the most superficial scanning field to 50  $\mu\text{m}$  below the deepest scanning field. Each plane was  $500 \times 800 \mu\text{m}$ , together tiling a  $800 \times 800 \mu\text{m}$  field of view (300  $\mu\text{m}$  total overlap), and repeated 100 times per plane.

**Visual stimulation** Visual stimuli were displayed on a 31.8  $\times$  56.5 cm (height  $\times$  width) HD widescreen LCD monitor with a refresh rate of 60 Hz at a resolution of  $1080 \times 1920$  pixels. When the monitor was centered on and perpendicular to the surface of the eye at the closest point, this corresponded to a visual angle of  $2.2^\circ/\text{cm}$  on the monitor. We recorded the voltage of a photodiode (TAOS TSL253) taped to the top left corner of the monitor to measure the gamma curve and luminance of the monitor before each experimental session. The voltage of the photodiode is linearly correlated with the luminance of the monitor. To convert from photodiode voltage to monitor luminance, we used a luminance meter (LS-100 Konica Minolta) to measure monitor luminance for 16 equidistant pixel values from 0-255 while recording the photodiode voltage. The gamma value for experiments in this paper ranged from 1.751 to 1.768 (mean = 1.759, standard deviation = 0.005). The minimum luminance ranged from 0.23  $\text{cd}/\text{m}^2$  to 0.97  $\text{cd}/\text{m}^2$  ( $0.49 \pm 0.25$ , mean  $\pm$  standard deviation), and the maximum ranged from 84.11  $\text{cd}/\text{m}^2$  to 86.04  $\text{cd}/\text{m}^2$  ( $85.07 \pm 0.72$ , mean  $\pm$  standard deviation).

**ImageNet stimulus.** Natural images were randomly selected from the ImageNet database (Deng et al., 2009), converted to gray scale, and cropped to the monitor aspect ratio of 16:9. To probe center-surround interactions, we modified the images using a circular mask that was approx. 48 degrees in visual angle in diameter with smoothed edges. The mask radius was defined as fraction of monitor width, i.e.  $r_{\text{aperture}} = 1$  means a full-field mask. We used  $r_{\text{aperture}} = 0.2$

$$r = \frac{r_{\text{pixel}} - r_{\text{aperture}}}{\alpha} + 1$$

$$M = \begin{cases} \frac{1 + \cos(\pi r)}{2} & 0 < r < 1 \\ 1 & r \leq 0 \\ 0 & \text{otherwise} \end{cases}$$

where  $M$  is the mask,  $r$  is the radius, and  $\alpha$  is the width of the transition. We presented 5,000 unique natural images without repetition during each scan, half of which were masked. We also presented the same 100 images repeated 10 times as full-field and 10 times as masked. The 100 images that were repeated were conserved across experiments, while the unique images varied across scans. Each trial consisted of one image presented for 500 ms with a preceding blanking period of 300 - 500 ms (randomly determined per trial).

**Eye tracking** A movie of the animal's eye and face was captured throughout the experiment. A hot mirror (Thorlabs

FM02) positioned between the animal's left eye and the stimulus monitor was used to reflect an IR image onto a camera (Genie Nano C1920M, Teledyne Dalsa) without obscuring the visual stimulus. The position of the mirror relative to the camera was manually adjusted if necessary per session to ensure that the camera focuses on the pupil. The field of view was manually cropped for each session. The field of view contained the left eye in its entirety, 282-300 pixels height  $\times$  378-444 pixels width at 20 Hz. Frame times were time stamped in the behavioral clock for alignment to the stimulus and scan frame times.

Light diffusing from the laser during scanning through the pupil was used to capture pupil diameter and eye movements. A DeepLabCut model (Mathis et al., 2018) was trained on 17 manually labeled samples from 11 animals to label each frame of the compressed eye video with 8 eyelid points and 8 pupil points at cardinal and intercardinal positions. Pupil points with likelihood  $>0.9$  (all 8 in  $93\% \pm 8\%$  of frames) were fit with the smallest enclosing circle, and the radius and center of this circle was extracted. Frames with  $<3$  pupil points with likelihood  $>0.9$  ( $0.7\% \pm 3\%$  frames per scan), or producing a circle fit with outlier  $>5.5$  standard deviations from the mean in any of the three parameters (center x, center y, radius,  $<1.3\%$  frames per scan) were discarded (total  $<3\%$  frames per scan). Trials affected by gaps in the frames were discarded ( $<2\%$  trials for all animals except one, where the animal's eye appeared irritated).

**Registrations of neurons in 3D stack** We densely sampled the imaging volume to avoid losing cells due to tissue deformation from day to day. Therefore, some cells were recorded in more than one plane. To select unique cells, we sub-sampled our recorded cells based on proximity in 3D space. Each functional scan plane was independently registered to the same 3D structural stack. Specifically, we used an affine transformation matrix with 9 parameters estimated via gradient ascent on the correlation between the sharpened average scanning plane and the extracted plane from the sharpened stack. Using the 3D centroids of all segmented cells, we iteratively grouped the closest two cells from different scans until all pairs of cells are at least  $10 \mu\text{m}$  apart or a further join produces an unrealistically tall mask ( $20 \mu\text{m}$  in z). Sequential registration of sections of each functional scan into the structural stack was performed to assess the level of drift in the z dimension. The drift over the 2 to 2.5 hour recording was  $4.70 \pm 2.64$ , and for most of them the drift was limited to  $<5 \mu\text{m}$ .

**Model architecture and training** The convolutional neural network used in this study consisted of two parts: a core and a readout. The core captured the nonlinear image representations and was shared among all neurons. The readout mapped the features of the core into neuronal responses and contained all neuron specific parameters.

**Core.** To get a rich set of nonlinear features, we used a deep CNN as our core. We used a CNN with 3 layers and 32 feature channels per layer as previously described in (Walker et al., 2019). These architectures were chosen with a hyper-

parameter search, with the objective of maximizing a validation score (see **Training and evaluation**). Each of the 2D convolutional layers was followed by a batch normalization layer and an ELU non-linearity.

**Readouts.** The goal of the readout was to find a linear-nonlinear mapping from the output of the last core layer  $\Phi(\mathbf{x})$  to a single scalar firing rate for every neuron. We used a pyramid readout, as described in Sinz et al. (2018). We computed a linear combination of the feature activations at a spatial position, parameterized as  $(x, y)$  relative coordinates (the middle of the feature map being  $(0, 0)$ ). Training this readout poses the challenge of maintaining gradient flow when optimizing the objective function. We tackled this challenge by recreating multiple sub-sampled versions of the feature maps and learning a common relative location for all of them. We then passed these features through a linear regression and a non-linearity to obtain the final neuronal responses.

**Training and evaluation.** Natural images in the training, validation and test sets were all Z-scored using the mean and standard deviation of the training set. The mean and standard deviation for the cropped natural images were weighted by the mask used to crop the images to avoid artificially lowering the mean and standard deviation due to large gray areas in the cropped images.

The networks were trained to minimize Poisson loss  $\frac{1}{m} \sum_{i=1}^m (\hat{r}^{(i)} - r^{(i)} \log \hat{r}^{(i)})$  where  $m$  denotes the number of neurons,  $\hat{r}$  the predicted neuronal response and  $r$  the observed response. We implemented early stopping on the correlation between predicted and measured neuronal responses on the validation set: if the correlation failed to increase during 10 consecutive epochs through the entire training set, we stopped the training and restored the best performing model over the course of training. After each stopping, we either decreased the learning rate or stopped training altogether if the number of learning-rate decay steps was reached. Network parameters were optimized via stochastic gradient descent using the Adam optimizer. Once training completed, the trained network was evaluated on the validation set to yield the score used for hyper-parameter selection.

**MEI and surround image generation** Because our neuronal recordings were performed with dense sampling (Z spacing =  $5 \mu\text{m}$ ), we first needed to select unique neurons. We registered the planes of the functional experiments to the stack of the volume (see **Registration of neurons in 3D stack**) and identified unique neurons.

Then, we optimized the MEIs and the surround images in two steps.

**MEI generation.** We used regularized gradient ascent by solving the optimization problem defined as

$$x^* = \arg \max_x f_i(x)$$

on our trained deep neural network models to obtain a maximally exciting input image for each neuron, given by  $x$

$$x \in \mathbb{R}^{n \times m}$$

(Walker et al., 2019). We initialized with a Gaussian white noise image. In each iteration of gradient ascent, we showed the image to the model and calculated the gradients of the image w.r.t. the model activation of a single neuron. We then blurred the obtained gradient with Gaussian blurring, with a Gaussian sigma of 1 pixel. Following this, we stepped our optimizer to change the image as given by the gradients. Finally, we calculated the standard deviation of the resulting image and compared it to a fixed budget of 0.05 for the MEI. The standard deviation budget can be effectively thought of as a contrast constraint. The contrast budget was chosen to minimize the number of pixels with values exceeding those corresponding to 0 and 255, which are the lower and upper bound for pixel values displayed on the monitor. We used the Stochastic Gradient Descent (SGD) optimizer with step size=0.1 and ran each optimization for 1,000 iterations.

**Surround image generation.** A tight mask (ranging between 0 and 1) around the MEI was computed by thresholding (see below) which we used to define the 'center' and set it apart from the 'surround' during the next step of optimization. By applying the inverse MEI mask to the target image  $x$ , we optimized the surrounding area in the image by allowing more contrast (RMS contrast = 0.1) outside of the MEI mask.

To define the center stimuli, we computed a mask around the MEI for each neuron by thresholding at 1.5 standard deviations above the mean. We then blurred the mask with Gaussian sigma = 1 pixel. We initialized an image with Gaussian noise and cropped out the center of this image using the MEI mask and added the MEI at a fixed contrast = 0.05. At the same time, we used the inverse of the MEI mask to set the contrast for the area outside of the mask to 0.1. A gradient was computed on the modified image and we blurred the gradient with a Gaussian sigma = 1. We used the same SGD optimizer to update the image at each iteration, and due to the inverse of the mask being applied to the image, only pixels outside of the MEI mask could be changed (illustrated in Fig. 2a). We set the full-field image contrast to an arbitrary value within the training image regime (0.1) to prevent the pixel values from getting out of range and this step was not differentiable. At the end of each iteration, we normalized the contrast in the center and the surround again to reach the optimal stimulus with correct contrast (MEI=0.05, surround=0.1). We repeated these steps for 1,000 iterations. To generate the extend mask for the MEI used in Suppl. Fig. 4, we set the value between 1 and 0.001, i.e. in the blurred area, in the original mask to 1 and blurred the new mask with the same Gaussian filter that was applied to the MEI mask. We applied the extended mask to the surround images to produce a new set of masked surround images that were slightly smaller than the original ones, and tested surround modulation restricted only to the 'near' surround region.

### Probabilistic model

**Hierarchical generative model.** We simulated inference using a simple probabilistic generative model of the stimulus as would be learned by the brain as an attempt to explain

our center-surround results. In our model,  $G$  is represented in a higher visual area, encoding a global orientation variable,  $X$  represents our model sensory neurons, each with an oriented Gabor filter as its projective field (PF), and  $I$  represents the visual input. We assume the existence of a single  $G \sim \mathcal{U}(0, \pi)$ . We model sensory neurons as  $X = \{x_i\}_{i=1}^{n_x}$ , where  $n_x$  is the number of sensory neurons ( $n_x = 6$  in our case), conditioned on  $G$  as  $x_i|G \sim \frac{1}{\lambda(i)} \exp\left(-\frac{x_i}{\lambda(i)}\right) H(x_i)$  where  $\lambda(i)$  is the firing rate function of the  $i$ th neuron defined by a von Mises function around the global orientation  $G$  as  $\lambda(i) = \exp\left(\kappa \frac{\cos(\theta_i - G)}{2\pi I_0(\kappa)}\right)$ , where  $\theta_i$  is the preferred orientation of the  $i$ th neuron. In other words, the closer the preferred orientation of a neuron to the global orientation, the higher is its firing rate. This way, we induce a positive (prior) correlation among neurons that prefer similar orientations, i.e. neurons with vertical PFs have high correlation with each other, as do neurons with horizontal PFs. Finally, the visual input in our model is assumed to be a noisy, linear combination of the Gabor PFs of neurons with neuronal activations, i.e.  $I \sim \mathcal{N}(I|\sum_i^{n_x} \text{PF}_i x_i, \sigma^2)$ , where  $\text{PF}_i$  is the PF and  $x_i$  is the activation (spike count) of the  $i$ th neuron.

**Inference.** Our assumption is that when presented with a visual input, the brain computes the posterior over variables  $X$  and  $G$  using the (learned) generative model, i.e. computes  $p(G, X|I)$ . We sampled from this posterior for various stimuli via No-U-Turn-Sampler (NUTS) using python's PyMC package. For each stimulus, we sampled 4,000 samples of  $G$  and each neuron  $x_i$  after a burn-in period of 1,000 samples. We then visualized the samples of the center neuron across different stimuli in Fig. 5d. We computed the mean of the samples of the center neuron for a given stimulus in order to quantify the effect that the particular stimulus had. The mean of the center neuron for the different stimuli reproduced our key experimental results: (1) the example neuron's mean was driven strongly by the MEI alone, (2) the spatially congruent stimulus drove the example neuron's mean in the center stronger than its MEI, (3) the spatially incongruent stimulus inhibited the mean of the samples of the neuron, despite the MEI being present in the center.

### Closed-loop experiments

**Selection of neurons for closed-loop.** We ranked the neurons recorded in one experiment based on the reliability and model performance (test correlation). Specifically, we correlated the leave-one-out mean response with the remaining single-trial response across repeated images in the test set to obtain a measurement of neuronal response reliability. We then computed an averaged rank score of each neuron from its reliability rank and model test correlation rank. After removing duplicate neurons following the procedure described above, we selected the top 150 neurons according to the averaged rank of the correlation between predicted response and observed response averaged over repeats and the correlation between the leave-one-out mean response of repeated test trials to the left-out test trial response for closed-loop experiments.

**Stimulus presentation.** We converted the images generated by the model back to pixel space by reversing the Z-score step with the stats of the training set. Each image was repeated 40 times. We shuffled all the images with repeats across different classes (MEI, excitatory and inhibitory surrounds and contrast-matched MEI, masked surround controls) and presented them at random orders. Each trial consisted of one image presented for 500 ms with a preceding blanking period of 300 - 500 ms (randomly determined per trial).

**Matching neurons across experiments.** We matched neurons from different experiments according to the spatial proximity in the volume of the same anatomical 3D stack. Each functional scan plane was registered to the 3D stacks collected after each day's experiment. We chose the neurons that had the highest matching frequency across all stacks, and included them as a valid neuron in the closed-loop analysis.

**Estimation of center RF size** To measure to size of the minimum response field (MRF) for each neuron, we presented stimuli consisting of circular bright (pixel value=255) and dark (pixel value=0) dots of size 7 degrees in visual angle on a gray background (pixel value=128) in conjunction with natural image stimuli. The dots were randomly shown at locations on a 9 by 9 grid covering 40% of the monitor in the center along the horizontal edge, and at each location, the dot was shown for 250 ms and repeated 16 times. The responses were averaged across repeats, and a 2D Gaussian was fitted to the On and Off response maps, respectively. The size of the MRF was measured as the largest distance between points on the border of the 2D Gaussian at 1.5 standard deviations away for both On and Off responses.

To estimate the size of the MEIs and the excitatory and inhibitory surround, we first computed the mask for each image as described in section **MEI and surround image generation**. The size was computed in pixels as the longest distance between points on the border of the mask. The size was converted to degrees in visual angle according to the ratio between pixel and degrees in visual angle.

**Exciting natural image patches and natural surrounds** All natural images in the ImageNet dataset were first Z-scored with the mean and standard deviation of the training dataset. We then cropped the images with the MEI masks and normalized to match the contrast of the MEI within the mask. The images were presented to the model to get the predicted response. Images that elicited activations above 80% of MEI activation were chosen as the maximally exciting natural image patches. Images used to train the specific model were removed from this collection. For neurons with more than 10 maximally exciting natural image patches, we replaced the center of the natural image with the MEI and included the surround region of the natural image to the same extend as the average size of the excitatory and the inhibitory surround.

**Representational similarity** The maximally exciting natural image patches of a neuron plus the surround of the same image were normalized to the same contrast as the excitatory and the inhibitory surround images and were presented to the

model. The excitatory and the inhibitory surround images were cropped with the average mask of the two to match the size, contrast-adjusted and presented to the model. The activation of all neurons in the model were taken as an approximation of the given image in 'representational space'. We computed Pearson correlation between a natural image patch with surround and an image of the MEI with either excitatory or inhibitory surround. The Pearson correlation is an estimation of 'representational similarity'.

**Auto-correlation function** To quantify correlations across space of optimized and natural center-surround images, we computed the auto-correlation function of each image (Rikhye and Sur, 2014). For each neuron, we first identified exciting natural images (>80 % activation relative to the MEI) with the preferred feature in the center as described above. We then cropped the optimized and exciting natural images based on the average mask of the excitatory and inhibitory surrounds, extracted horizontal and vertical intensity profiles through the center of mass of each image and computed the mean auto-correlation function of these intensity projections for excitatory and inhibitory center-surround images, as well as for all exciting natural images per cell. We shifted the intensity projections in steps of 2 degrees visual angle and for maximally 20 degrees visual angle, thereby extending beyond the MEI (radius approx. 15 degrees visual angle) into the surround.

**Extrapolated surround images** We generated extrapolated surround images based on the spatial pattern of the MEI using a bivariate spline interpolation method on a rectangular grid (*RectBivariateSpline* function of *scipy* package). Specifically, we first cropped out the MEI using a 95% threshold of the MEI mask and fit the cropped MEI with the *RectBivariateSpline* function. Then, we used the fit to extrapolate from the MEI into the surround and cropped the extrapolated surround based on the mask of optimized surround images.

**Replication of center-surround modulation in functional connectomics dataset** Recently, we and others released a large-scale functional connectomics dataset of mouse visual cortex ("MICrONS dataset"), including responses of >75k neurons to full-field natural movies and the reconstructed sub-cellular connectivity of the same cells from electron microscopy data (MICrONS Consortium et al., 2021). A dynamic recurrent neural network (RNN) model of this mouse's visual cortex—digital twin—exhibits not only a high predictive performance for natural movies, but also accurate out-of-domain performance on other stimulus classes such as drifting Gabor filters, directional pink noise, and random dot kinematograms (Wang et al., 2023). Here, we took advantage of the model's ability to generalize to other visual stimulus domains and presented our full-field and masked images to this digital twin model in order to relate specific functional properties to the neurons' connectivity and anatomical properties. Specifically, we recorded the visual activity of the same neuronal population to static natural images as well as to the identical natural movies that were used in the

MICrONS dataset. Neurons were matched anatomically as described for the closed loop experiments. Based on the responses to static natural images we trained a static model as described above, and from the responses to natural movies we trained a dynamic model using a RNN architecture described in (Wang et al., 2023). We then presented the same static natural image set that we showed to the mice also to their dynamic model counterparts and trained a second static model using these predicted in silico responses. This enabled us to compare the MEIs and surround images for the same neurons generated from two different static models: one trained directly on responses from real neurons, and another trained on synthetic responses to static images from dynamic models (D-MEI and D-surround). To quantify similarity, we presented both versions of MEIs and surround images to an independent static model trained on the same natural images and responses but initialized with a different random seed, thereby avoiding model-specific biases.

**Code and data availability** The analysis code and all data will be publicly available in an online repository latest upon journal publication. Please contact us if you would like access before that time.

#### ACKNOWLEDGEMENTS

The authors thank David Markowitz, the IARPA MICrONS Program Manager, who coordinated this work during all three phases of the MICrONS program. We thank IARPA program managers Jacob Vogelstein and David Markowitz for co-developing the MICrONS program. We thank Jennifer Wang, IARPA SETA for her assistance. The work was supported by the Intelligence Advanced Research Projects Activity (IARPA) via Department of Interior/ Interior Business Center (DoI/IBC) contract numbers D16PC00003, D16PC00004, and D16PC00005. The U.S. Government is authorized to reproduce and distribute reprints for Governmental purposes notwithstanding any copyright annotation thereon. XP acknowledges support from NSF CAREER grant IOS-1552868. XP and AST acknowledge support from NSF NeuroNex grant 1707400. AST also acknowledges support from National Institute of Mental Health and National Institute of Neurological Disorders and Stroke under Award Number U19MH114830 and National Eye Institute/National Institutes of Health Core Grant for Vision Research (no. T32-EY-002520-37). Disclaimer: The views and conclusions contained herein are those of the authors and should not be interpreted as necessarily representing the official policies or endorsements, either expressed or implied, of IARPA, DoI/IBC, or the U.S. Government.

This work was also supported by the German Research Foundation (to FHS: SFB 1233, Robust Vision: Inference Principles and Neural Mechanisms, TP06, project number 276693517; to ASE: SFB 1456, project B05, project number 432680300), the European Research Council (ERC) under the European Union's Horizon Europe research and innovation programme (AEH, grant agreement number 101041669), the National Eye Institute (to RH: 5R01EY028811).

#### AUTHOR CONTRIBUTIONS

**JK:** Conceptualization, Methodology, Validation, Software, Formal Analysis, Investigation, Writing - Original Draft, Visualization, Project administration; **SS:** Conceptualization, Formal Analysis, Writing - Original Draft, Visualization; **KP, TM:** Investigation, Validation; **ZhuD, EW:** Investigation, Validation, Methodology (dynamic model and functional connectomics); **ZhiD, DTT:** Conceptualization, Methodology, Visualization (dynamic model and functional connectomics); **PGF, SiP, SaP, JR:** Investigation, Validation, Methodology (functional connectomics); **ASE, XP:** Conceptualization, Writing - Review & Editing, Funding acquisition; **RMH:** Conceptualization, Methodology, Funding acquisition, Writing - Review & Editing; **FHS:** Conceptualization, Writing - Review & Editing, Supervision, Funding acquisition; **KF:** Conceptualization, Formal Analysis, Supervision, Visualization, Writing - Original draft, Project administration; **AST:** Conceptualization, Experimental and analysis design, Supervision, Funding acquisition, Writing - Review & Editing, Project administration

## Reference

- H. Adesnik, W. Bruns, H. Taniguchi, Z. J. Huang, and M. Scanziani. A neural circuit for spatial summation in visual cortex. *Nature*, 490(7419):226–31, 2012. ISSN 1476-4687. doi: 10.1038/nature11526.
- H. J. Alitto and W. M. Usrey. Origin and dynamics of extraclassical suppression in the lateral geniculate nucleus of the macaque monkey. *Neuron*, 57(1):135–146, Jan. 2008.
- J. Allman, F. Miezin, and E. McGuinness. Stimulus specific responses from beyond the classical receptive field: neurophysiological mechanisms for local-global comparisons in visual neurons. *Annu. Rev. Neurosci.*, 8:407–430, 1985.

- M. Bányai, A. Lazar, L. Klein, J. Klon-Lipok, M. Stippinger, W. Singer, and G. Orbán. Stimulus complexity shapes response correlations in primary visual cortex. *Proceedings of the National Academy of Sciences*, 116(7):2723–2732, 2019.
- H. B. Barlow, C. Blakemore, and J. D. Pettigrew. The neural mechanism of binocular depth discrimination. *The Journal of physiology*, 193(2):327–342, 1967. ISSN 0022-3751. doi: 10.1113/jphysiol.1967.sp008360.
- P. Bashivan, K. Kar, and J. J. DiCarlo. Neural population control via deep image synthesis. *Science (New York, N.Y.)*, 364(6439), 2019. ISSN 1095-9203. doi: 10.1126/science.aav9436.
- I. Biederman, R. J. Mezzanotte, and J. C. Rabinowitz. Scene perception: detecting and judging objects undergoing relational violations. *Cogn. Psychol.*, 14(2):143–177, Apr. 1982.
- W. H. Bosking, Y. Zhang, B. Schofield, and D. Fitzpatrick. Orientation selectivity and the arrangement of horizontal connections in tree shrew striate cortex. *J. Neurosci.*, 17(6):2112–2127, Mar. 1997.
- J. R. Cavanaugh, W. Bair, and J. A. Movshon. Nature and interaction of signals from the receptive field center and surround in macaque V1 neurons. *J. Neurophysiol.*, 88(5):2530–2546, Nov. 2002a.
- J. R. Cavanaugh, W. Bair, and J. A. Movshon. Nature and Interaction of Signals From the Receptive Field Center and Surround in Macaque V1 Neurons. *Journal of Neurophysiology*, 88(5):2530–2546, 2002b. ISSN 0022-3077. doi: 10.1152/jn.00692.2001.
- J. R. Cavanaugh, W. Bair, and J. A. Movshon. Selectivity and Spatial Distribution of Signals From the Receptive Field Surround in Macaque V1 Neurons. *Journal of Neurophysiology*, 88(5):2547–2556, 2002c. ISSN 0022-3077. doi: 10.1152/jn.00693.2001.
- C.-C. Chiao and R. H. Masland. Contextual tuning of direction-selective retinal ganglion cells. *Nat. Neurosci.*, 6(12):1251–1252, Dec. 2003.
- R. Coen-Cagli, A. Kohn, and O. Schwartz. Flexible gating of contextual influences in natural vision. *Nat. Neurosci.*, 18(11):1648–1655, Nov. 2015.
- S. V. David, W. E. Vinje, and J. L. Gallant. Natural stimulus statistics alter the receptive field structure of v1 neurons. *J. Neurosci.*, 24(31):6991–7006, Aug. 2004.
- J. Deng, W. Dong, R. Socher, L.-J. Li, K. Li, and L. Fei-Fei. ImageNet: A Large-Scale Hierarchical Image Database. In *CVPR09*, 2009.
- J. Fiser, P. Berkes, G. Orbán, and M. Lengyel. Statistically optimal perception and learning: from behavior to neural representations. *Trends in cognitive sciences*, 14(3):119–130, 2010.
- K. Franke, K. F. Willeke, K. Ponder, M. Galdamez, N. Zhou, T. Muhammad, S. Patel, E. Froudarakis, J. Reimer, F. H. Sinz, and A. S. Tolia. State-dependent pupil dilation rapidly shifts visual feature selectivity. *Nature*, 610(7930):128–134, 2022. ISSN 14764687. doi: 10.1038/s41586-022-05270-3.
- E. Froudarakis, P. Berens, A. S. Ecker, R. J. Cotton, F. H. Sinz, D. Yatsenko, P. Saggau, M. Bethge, and A. S. Tolia. Population code in mouse V1 facilitates readout of natural scenes through increased sparseness. *Nature Neuroscience*, 17(6):851–857, 2014. ISSN 15461726. doi: 10.1038/nm.3707.
- M. E. Garrett, I. Nauhaus, J. H. Marshel, and E. M. Callaway. Topography and Areal Organization of Mouse Visual Cortex. *Journal of Neuroscience*, 34(37):12587–12600, 2014. ISSN 0270-6474. doi: 10.1523/JNEUROSCI.1124-14.2014.
- W. S. Geisler, J. S. Perry, B. J. Super, and D. P. Gallogly. Edge co-occurrence in natural images predicts contour grouping performance. *Vision Research*, 41(6):711–724, 2001. ISSN 0042-6989. doi: 10.1016/S0042-6989(00)00277-7.
- A. Giovannucci, J. Friedrich, P. Gunn, J. Kalton, B. L. Brown, S. A. Koay, J. Taxisis, F. Najafi, J. L. Gauthier, P. Zhou, B. S. Khakh, D. W. Tank, D. B. Chklovskii, and E. A. Pnevmatikakis. Caiman an open source tool for scalable calcium imaging data analysis. *eLife*, 8:1–45, 2019. ISSN 2050084X. doi: 10.7554/eLife.38173.
- M. A. Goldin, B. Lefebvre, S. Virgili, M. K. Pham Van Cang, A. Ecker, T. Mora, U. Ferrari, and O. Marre. Context-dependent selectivity to natural images in the retina. *Nat. Commun.*, 13(1):5556, Sept. 2022.
- R. M. Haefner, P. Berkes, and J. Fiser. Perceptual decision-making as probabilistic inference by neural sampling. *Neuron*, 90(3):649–660, 2016.
- H. S. Hock, G. P. Gordon, and R. Whitehurst. Contextual relations: The influence of familiarity, physical plausibility, and belongingness. *Percept. Psychophys.*, 16(1):4–8, Jan. 1974.
- M. F. Iacaruso, I. T. Gasler, and S. B. Hofer. Synaptic organization of visual space in primary visual cortex. *Nature*, 547(7664):449–452, 2017. ISSN 0028-0836. doi: 10.1038/nature23019.
- H. E. Jones, K. L. Grieve, W. Wang, and A. M. Sillito. Surround suppression in primate V1. *J. Neurophysiol.*, 86(4):2011–2028, Oct. 2001.
- H. E. Jones, I. M. Andolina, B. Ahmed, S. D. Shipp, J. T. C. Clements, K. L. Grieve, J. Cudeiro, T. E. Salt, and A. M. Sillito. Differential feedback modulation of center and surround mechanisms in parvocellular cells in the visual thalamus. *J. Neurosci.*, 32(45):15946–15951, Nov. 2012.
- J. P. Jones and L. A. Palmer. The two-dimensional spatial structure of simple receptive fields in cat striate cortex. *J. Neurophysiol.*, 58(6):1187–1211, Dec. 1987.
- M. K. Kapadia, M. Ito, C. D. Gilbert, and G. Westheimer. Improvement in visual sensitivity by changes in local context: Parallel studies in human observers and in V1 of alert monkeys. *Neuron*, 15(4):843–856, 1995. ISSN 08966273. doi: 10.1016/0896-6273(95)90175-2.
- M. K. Kapadia, G. Westheimer, and C. D. Gilbert. Dynamics of spatial summation in primary visual cortex of alert monkeys. *Proceedings of the National Academy of Sciences of the United States of America*, 96(21):12073–12078, 1999. ISSN 0027-8424. doi: 10.1073/pnas.96.21.12073.
- A. J. Keller, M. Dipoppa, M. M. Roth, M. S. Caudill, A. Ingrassio, K. D. Miller, and M. Scanziani. A Disinhibitory Circuit for Contextual Modulation in Primary Visual Cortex. *Neuron*, 108(6):1181–1193.e8, 2020a. ISSN 10974199. doi: 10.1016/j.neuron.2020.11.013.
- A. J. Keller, M. M. Roth, and M. Scanziani. Feedback generates a second receptive field in neurons of the visual cortex. *Nature*, (June 2019):1–5, 2020b. ISSN 0028-0836. doi: 10.1038/s41586-020-2319-4.
- G. B. Keller and T. D. Mrsic-Flogel. Predictive processing: A canonical cortical computation. *Neuron*, 100(2):424–435, Oct. 2018.
- D. Kersten, P. Mamassian, and A. Yuille. Object perception as bayesian inference. *Annu. Rev. Psychol.*, 55:271–304, 2004.
- J. J. Knierim and D. C. Van Essen. Neuronal responses to static texture patterns in area V1 of the alert macaque monkey. *Journal of Neurophysiology*, 67(4):961–980, 1992. ISSN 00223077. doi: 10.1152/jn.1992.67.4.961.

- D. C. Knill and W. Richards. *Perception as Bayesian inference*. Cambridge University Press, 1996.
- N. Kriegeskorte, M. Mur, and P. Bandettini. Representational similarity analysis - connecting the branches of systems neuroscience. *Front. Syst. Neurosci.*, 2:4, Nov. 2008.
- T. S. Lee and D. Mumford. Hierarchical bayesian inference in the visual cortex. *J. Opt. Soc. Am. A Opt. Image Sci. Vis.*, 20(7):1434–1448, July 2003.
- T. S. Lee and M. Nguyen. Dynamics of subjective contour formation in the early visual cortex. *Proceedings of the National Academy of Sciences of the United States of America*, 98(4):1907–1911, 2001. ISSN 00278424. doi: 10.1073/pnas.98.4.1907.
- J. B. Levitt and J. S. Lund. Contrast dependence of contextual effects in primate visual cortex. *Nature*, 387:73–76, 1997. ISSN 0028-0836. doi: 10.1038/387073a0.
- W. Li, V. Piëch, and C. D. Gilbert. Contour Saliency in Primary Visual Cortex. *Neuron*, 50(6):951–962, 2006. ISSN 08966273. doi: 10.1016/j.neuron.2006.04.035.
- T. Lochmann and S. Deneve. Neural processing as causal inference. *Current opinion in neurobiology*, 21(5):774–781, 2011.
- K.-K. Lurz, M. Bashiri, K. Willeke, A. Jagadish, E. Wang, E. Y. Walker, S. A. Cadena, T. Muhammad, E. Cobos, A. S. Tolia, A. S. Ecker, and F. H. Sinz. Generalization in data-driven models of primary visual cortex. In *International Conference on Learning Representations*, 2021.
- A. Mathis, P. Mamianna, K. M. Cury, T. Abe, V. N. Murthy, M. W. Mathis, and M. Bethge. DeepLabCut: markerless pose estimation of user-defined body parts with deep learning. *Nat. Neurosci.*, 21(9):1281–1289, Aug. 2018.
- MICrONS Consortium, J. Alexander Bae, M. Baptiste, A. L. Bodor, D. Brittain, J. Buchanan, D. J. Bumbarger, M. A. Castro, B. Celii, E. Cobos, F. Collman, N. M. da Costa, S. Dorkenwald, L. Elabbady, P. G. Fahey, T. Fliss, E. Froudarakis, J. Gager, C. Gamlin, A. Halageri, J. Hebditch, Z. Jia, C. Jordan, D. Kapner, N. Kemnitz, S. Kinn, S. Koolman, K. Kuehner, K. Lee, K. Li, R. Lu, T. Macrina, G. Mahalingam, S. McReynolds, E. Miranda, E. Mitchell, S. S. Mondal, M. Moore, S. Mu, T. Muhammad, B. Nehoran, O. Ogedengbe, C. Papadopoulos, S. Papadopoulos, S. Patel, X. Pitkow, S. Popovych, A. Ramos, R. Clay Reid, J. Reimer, C. M. Schneider-Mizell, H. Sebastian Seung, B. Silverman, W. Silversmith, A. Sterling, F. H. Sinz, C. L. Smith, S. Suckow, M. Takeno, Z. H. Tan, A. S. Tolia, R. Torres, N. L. Turner, E. Y. Walker, T. Wang, G. Williams, S. Williams, K. Willie, R. Willie, W. Wong, J. Wu, C. Xu, R. Yang, D. Yatsenko, F. Ye, W. Yin, and S.-C. Yu. Functional connectomics spanning multiple areas of mouse visual cortex. *bioRxiv*, page 2021.07.28.454025, Aug. 2021.
- J. J. Nassi, S. G. Lomber, and R. T. Born. Corticocortical feedback contributes to surround suppression in V1 of the alert primate. *The Journal of neuroscience : the official journal of the Society for Neuroscience*, 33(19):8504–17, 2013. ISSN 1529-2401. doi: 10.1523/JNEUROSCI.5124-12.2013.
- C. M. Niell and M. P. Stryker. Modulation of visual responses by behavioral state in mouse visual cortex. *Neuron*, 65(4):472–479, Feb. 2010.
- L. Nurminen, S. Merlin, M. Bijanzadeh, F. Federer, and A. Angelucci. Top-down feedback controls spatial summation and response amplitude in primate visual cortex. *Nature Communications*, 9(2281), 2018. ISSN 2041-1723. doi: 10.1038/s41467-018-04500-5.
- A. Pasupathy and C. E. Connor. Shape representation in area v4: position-specific tuning for boundary conformation. *J. Neurophysiol.*, 86(5):2505–2519, Nov. 2001.
- U. Poiat, K. Mizobe, M. W. Pettet, T. Kasamatsu, and a. M. Norcia. Collinear stimuli regulate visual responses depending on cell's contrast threshold. *Nature*, 391(6667):580–584, 1998. ISSN 0028-0836. doi: 10.1038/35372.
- R. P. N. Rao and D. H. Ballard. Predictive coding in the visual cortex: a functional interpretation of some extra-classical receptive-field effects. *Nat. Neurosci.*, 2(1):79–87, Jan. 1999.
- J. Reimer, E. Froudarakis, C. R. Cadwell, D. Yatsenko, G. H. Denfield, and A. S. Tolia. Pupil Fluctuations Track Fast Switching of Cortical States during Quiet Wakefulness. *Neuron*, 84(2):355–362, 2014. ISSN 10974199. doi: 10.1016/j.neuron.2014.09.033.
- R. V. Rikhye and M. Sur. The spatial structure of correlations in natural scenes shapes neural coding in mouse primary visual cortex. *BMC Neurosci.*, 15(1):1–2, July 2014.
- A. F. Rossi, R. Desimone, and L. G. Ungerleider. Contextual modulation in primary visual cortex of macaques. *J. Neurosci.*, 21(5):1698–1709, Mar. 2001.
- J. M. Samonds, B. D. Feese, T. S. Lee, and S. Kuhlman. Non-uniform surround suppression of visual responses in mouse V1. *Journal of Neurophysiology*, page jn.00172.2017, 2017. ISSN 0022-3077. doi: 10.1152/jn.00172.2017.
- M. P. Sceniak, D. L. Ringach, M. J. Hawken, and R. M. Shapley. Contrast's effect on spatial summation by macaque V1 neurons. *Nature neuroscience*, 2(8):733–9, 1999. ISSN 1097-6256. doi: 10.1038/11197.
- K. E. Schmidt, R. Goebel, S. Löwel, and W. Singer. The perceptual grouping criterion of colinearity is reflected by anisotropies of connections in the primary visual cortex. *Eur. J. Neurosci.*, 9(5):1083–1089, May 1997.
- S. Schuett, T. Bonhoeffer, and M. Hübener. Mapping retinotopic structure in mouse visual cortex with optical imaging. *J. Neurosci.*, 22(15):6549–6559, Aug. 2002.
- O. Schwartz and E. P. Simoncelli. Natural signal statistics and sensory gain control. *Nat. Neurosci.*, 4(8):819–825, Aug. 2001.
- M. W. Self, J. a. M. Lorteije, J. Vangeneugden, E. H. van Beest, M. E. Grigore, C. N. Levell, J. a. Heemel, and P. R. Roelfsema. Orientation-Tuned Surround Suppression in Mouse Visual Cortex. *Journal of Neuroscience*, 34(28):9290–9304, 2014. ISSN 0270-6474. doi: 10.1523/JNEUROSCI.5051-13.2014.
- S. Shen, X. Jiang, F. Scala, J. Fu, P. Fahey, D. Kobak, Z. Tan, N. Zhou, J. Reimer, F. Sinz, and A. S. Tolia. Distinct organization of two cortico-cortical feedback pathways. *Nature Communications*, 13(1), 2022. ISSN 20411723. doi: 10.1038/s41467-022-33883-9.
- M. Sigman, G. A. Cecchi, C. D. Gilbert, and M. O. Magnasco. On a common circle: Natural scenes and gestalt rules. *Proceedings of the National Academy of Sciences of the United States of America*, 98(4):1935–1940, 2001. ISSN 00278424. doi: 10.1073/pnas.98.4.1935.
- L. C. Sincich and G. G. Blasdel. Oriented axon projections in primary visual cortex of the monkey. *J. Neurosci.*, 21(12):4416–4426, June 2001.
- F. H. Sinz, A. S. Ecker, P. G. Fahey, E. Y. Walker, E. Cobos, E. Froudarakis, D. Yatsenko, X. Pitkow, J. Reimer, and A. S. Tolia. Stimulus domain transfer in recurrent models for large scale cortical population prediction on video. *BioRxiv*, page 452672, 2018.
- N. J. Sofroniew, D. Flickinger, J. King, and K. Svoboda. A large field of view two-photon mesoscope with subcellular resolution for in vivo imaging. *eLife*, 5(JUN2016):1–20, 2016. ISSN 2050084X. doi: 10.7554/eLife.14472.
- I. Ustyuzhaninov, M. F. Burg, S. A. Cadena, J. Fu, T. Muhammad, K. Ponder, E. Froudarakis, Z. Ding, M. Bethge, A. S. Tolia, and A. S. Ecker. Digital twin reveals combinatorial code of non-linear computations in the mouse primary visual cortex. *bioRxiv*, page 2022.02.10.479884, 2022.
- W. E. Vinje and J. L. Gallant. Sparse coding and decorrelation in primary visual cortex during natural vision. *Science*, 287(5456):1273–1276, Feb. 2000.
- H. Von Helmholtz. *Handbuch der physiologischen Optik*, volume 9. Voss, 1867.
- E. Y. Walker, F. H. Sinz, E. Cobos, T. Muhammad, E. Froudarakis, P. G. Fahey, A. S. Ecker, J. Reimer, X. Pitkow, and A. S. Tolia. Inception loops discover what excites neurons most using deep predictive models. *Nature Neuroscience*, 22(December), 2019. ISSN 15461726. doi: 10.1038/s41593-019-0517-x.
- E. Y. Wang, P. G. Fahey, K. Ponder, Z. Ding, T. Muhammad, S. Patel, K. Franke, A. S. Ecker, J. Reimer, X. Pitkow, F. H. Sinz, and A. S. Tolia. Towards a foundation model of the mouse visual cortex. In preparation, 2023.
- K. F. Willeke, P. G. Fahey, M. Bashiri, L. Pede, M. F. Burg, C. Blessing, S. A. Cadena, Z. Ding, K.-K. Lurz, K. Ponder, T. Muhammad, S. S. Patel, A. S. Ecker, A. S. Tolia, and F. H. Sinz. The Sensorium competition on predicting large-scale mouse primary visual cortex activity. *arXiv*, pages 1–13, 2022.



## Supplementary Information

Supplemental Fig. 1 - Comparison of stimulus contrast of MEIs and excitatory and inhibitory surround

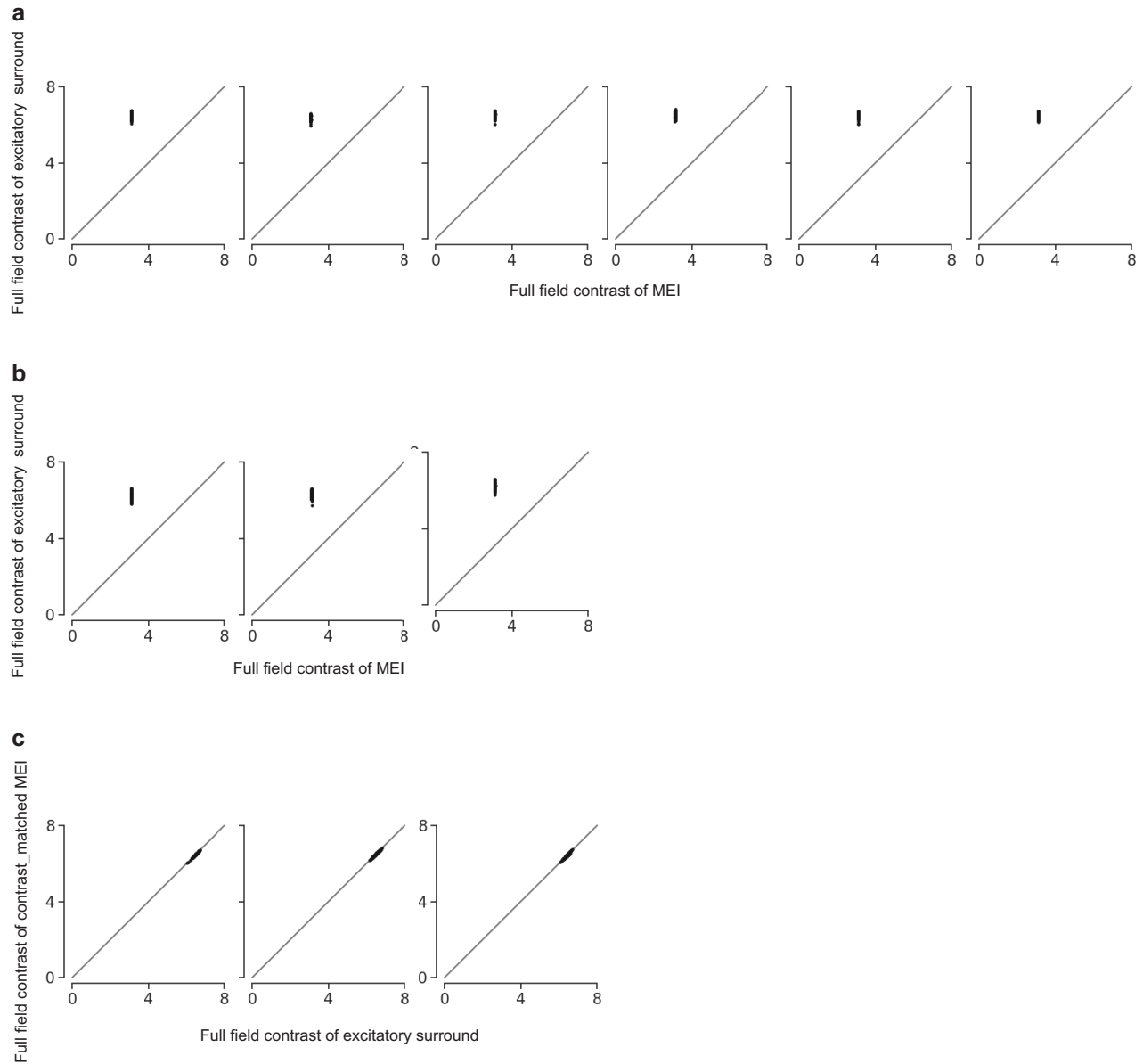
Supplemental Fig. 2 - Neuronal responses to MEIs and surround images recorded during inception loop experiments

Supplemental Fig. 3 - Contextual modulation is reproduced in digital twin of large-scale functional connectomics dataset

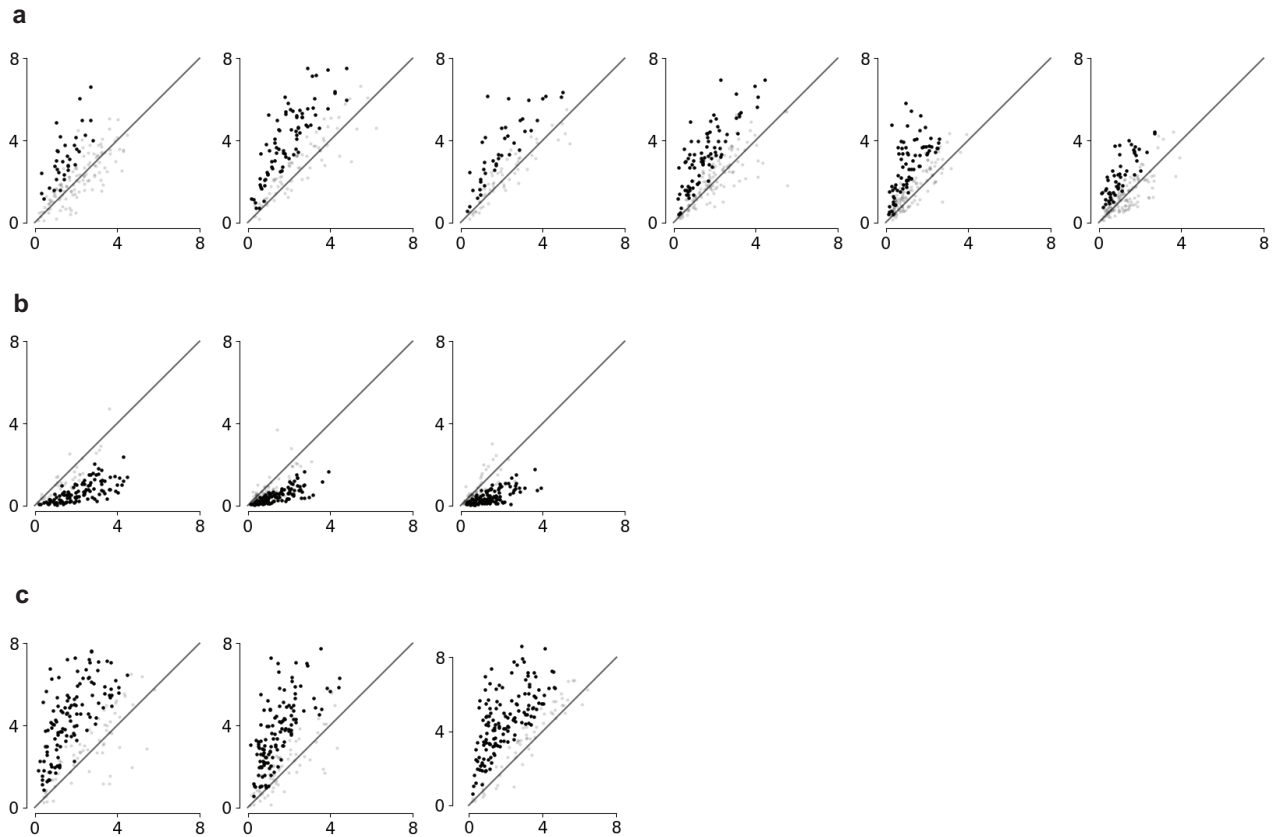
Supplemental Fig. 4 - Images restricted to the far surround still result in surround modulation

Supplemental Fig. 5 - Contrast-matched MEIs result in higher activation than MEIs with excitatory surround

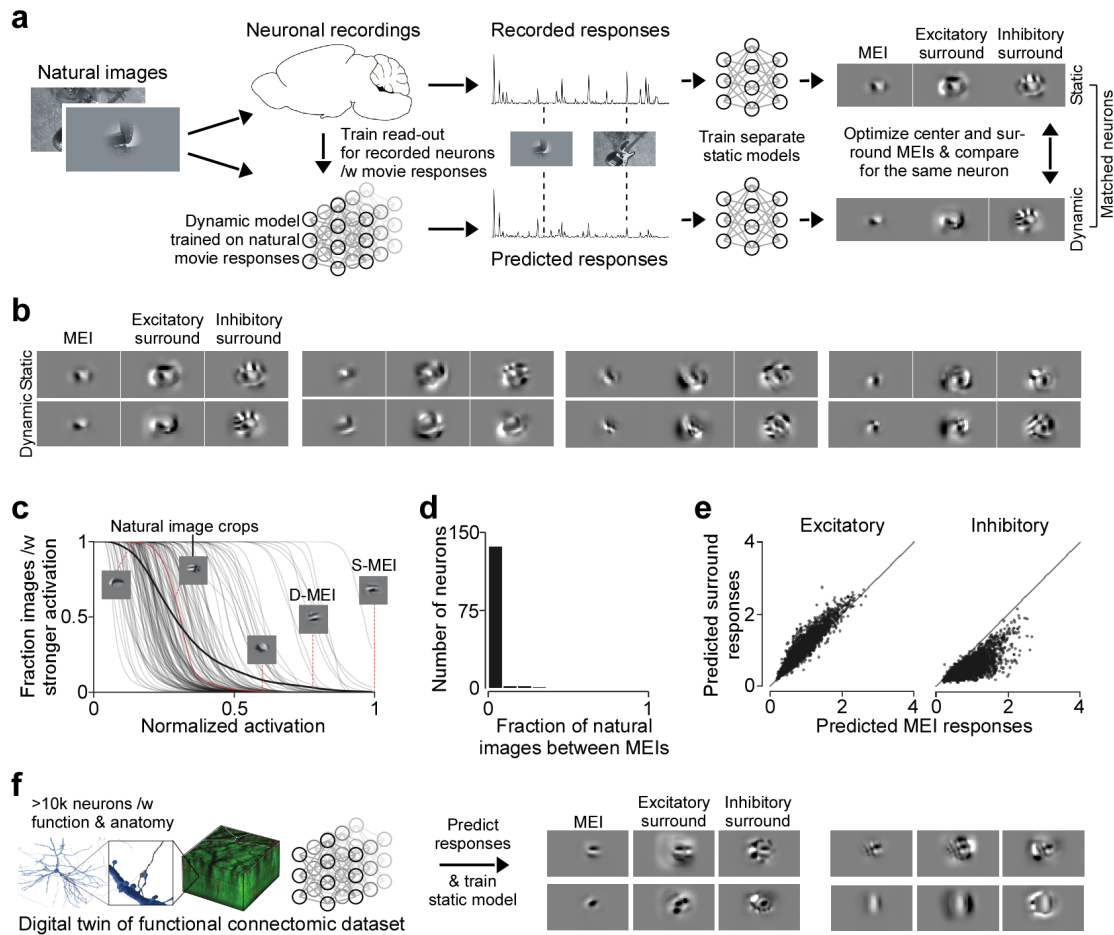
Supplemental Fig. 6 - Surround images extrapolated from the spatial pattern of the MEI



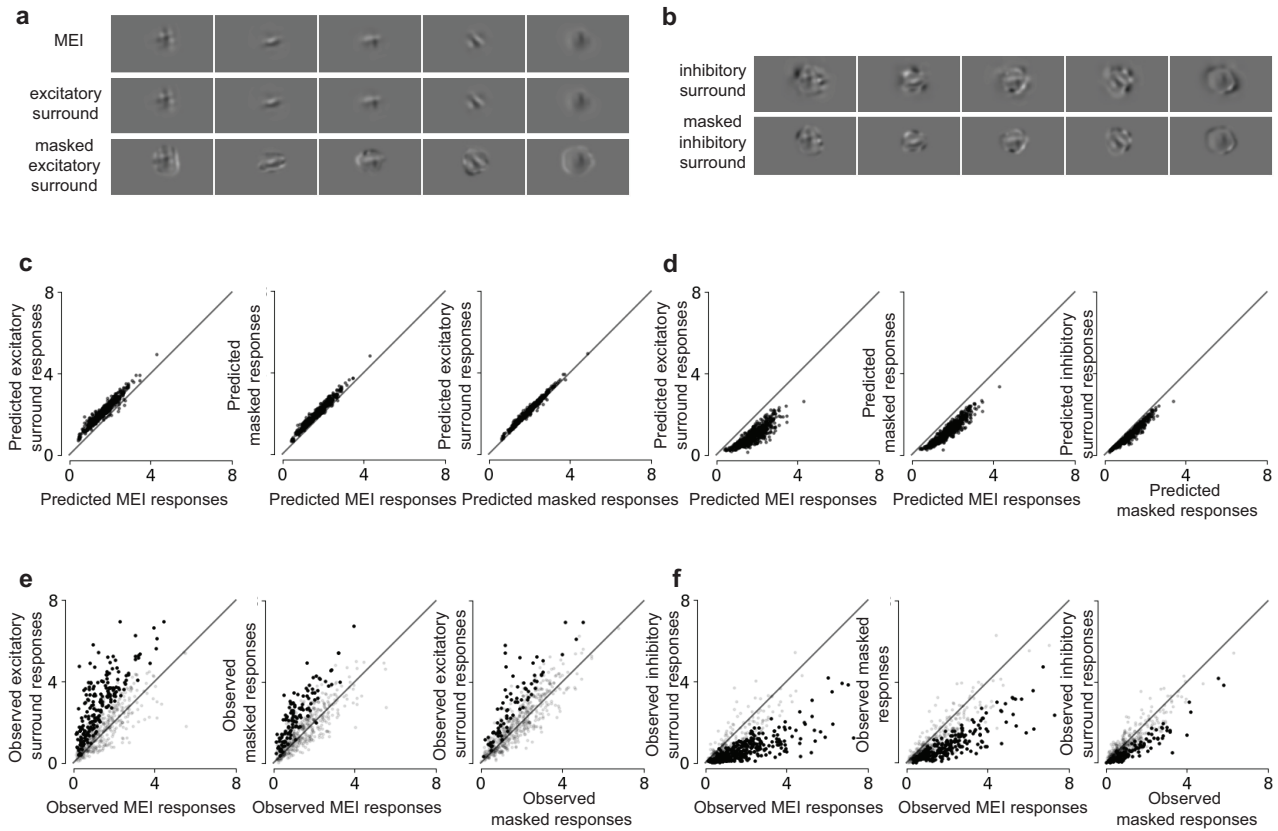
**Supplemental Fig. 1. Comparison of stimulus contrast of MEIs and excitatory and inhibitory surround.** **a**, Full-field RMS contrast comparison between the MEI (x-axis) and the excitatory surround images (y-axis) (n=6 animals, 960 cells total). **b**, Full-field RMS contrast comparison between the MEI (x-axis) and the inhibitory surround images (y-axis) (n=3 animals, 510 cells total). **c**, Full-field RMS contrast comparison between the excitatory surround image (x-axis) and the contrast-matched MEI (y-axis) (n=3 animals, 560 cells total).



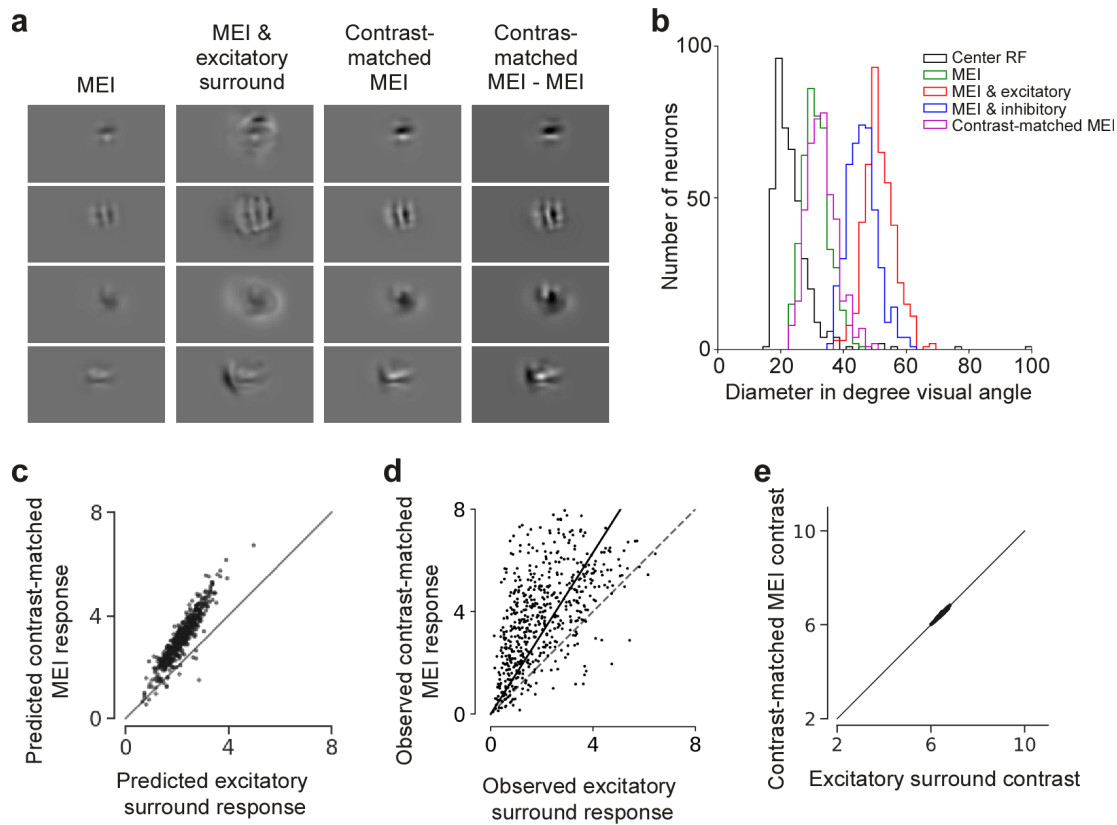
**Supplemental Fig. 2. Neuronal responses to MEIs and surround images recorded during inception loop experiments.** **a**, Comparing observed responses to the MEI (x-axis) and the excitatory surround (y-axis) per experiment (n=6 mice, 960 cells total). Dark dots indicate neurons where the response to the surround images is significantly higher than to the MEI (Wilcoxon rank-sum test, p-value<0.05). Across the population, the modulation was significant for all animals (p-value<0.05, Wilcoxon signed rank test). **b**, Comparing observed responses to the MEI (x-axis) and the inhibitory surround (y-axis) per experiment (n=3 mice, 510 cells total). Dark dots indicate neurons where the response to the surround images is significantly lower than to the MEI (Wilcoxon rank-sum test, p-value<0.05). Across the population, the modulation was significant for all animals (p-value<0.05, Wilcoxon signed rank test). **c**, Comparing observed responses to the excitatory surround (x-axis) and the contrast-matched MEI (y-axis) per experiment (n=3 mice, 560 cells total). Dark dots indicate neurons where the response to the contrast-matched MEIs is significantly higher than to the MEI (Wilcoxon rank-sum test, p-value<0.05). Across the population, the modulation was significant for all animals (p-value<0.05, Wilcoxon signed rank test).



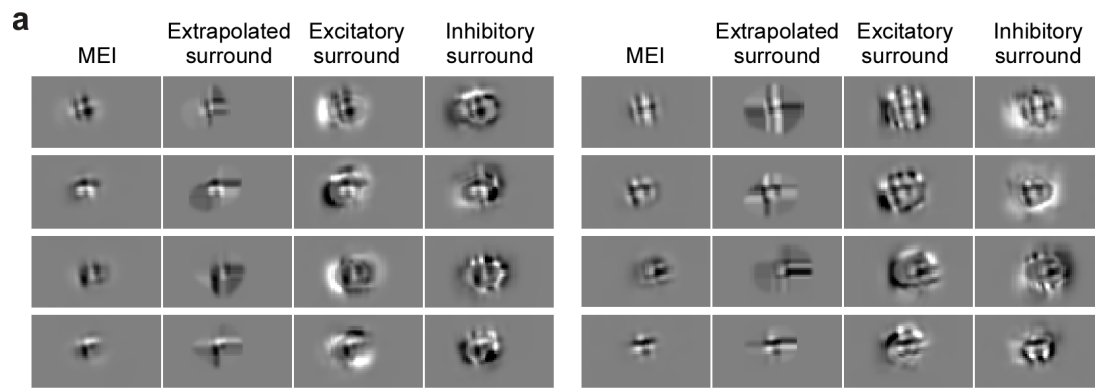
**Supplemental Fig. 3. Contextual modulation is reproduced in digital twin of large-scale functional connectomics dataset.** **a**, Circuit-level mechanistic explanations of neuronal function require the combination of functional recordings and anatomical analyses. This panel shows a schematic illustrating how we reproduced our findings regarding contextual modulation in a functional connectomic dataset, which includes responses of >75k neurons to full-field natural movies and the reconstructed sub-cellular connectivity of the same cells from electron microscopy data ("MICrONS" dataset (MICrONS Consortium et al., 2021)). Importantly, a dynamic model of this mouse visual cortex—digital twin—exhibits not only a high predictive performance for natural movies, but also accurate out-of-domain performance on other stimulus classes such as drifting Gabor filters, directional pink noise, and random dot kinematograms, allowing to present new stimuli to this digital twin model in order to relate specific functional properties to the neurons' connectivity and anatomical properties. To this end, we recorded the visual activity of the same neuronal population to static natural images as well as to the identical natural movies that were used in the MICrONS dataset. Based on the responses to static natural images we trained a static model as described above, and from the responses to natural movies we trained a dynamic model using a recurrent neural network architecture described in REF. We then presented the same static natural image set that we showed to the mice also to their dynamic model counterparts and trained a second static model using these predicted *in silico* responses. This enabled us to compare the MEIs and surround images for the same neurons generated from two different static models: one trained directly on responses from real neurons, and another trained on synthetic responses to static images from dynamic models (D-MEI and D-surround). **b**, Static and dynamic MEIs and surround images of four example neurons, matched across recordings using their anatomical position in a structural stack. Importantly, the MEIs and surround images optimized from these two models were perceptually very similar. **c**, To quantify this similarity, we presented both versions of MEIs and surround images to an independent static model trained on the same natural images and responses but initialized with a different random seed, thereby avoiding model-specific biases. The panel shows neuronal activation to natural image crops, normalized with respect to MEI activation. Gray lines show the fraction out of 5,000 images that elicit a given activation or higher for  $n=x$  example model neurons (mean in black). For a representative cell (red), we show MEI, D-MEI and image crops with different activations. **d**, Fraction of natural images that activate the neurons stronger than the D-MEIs. On the population level, the fraction of natural image crops with activations higher than the D-MEI was very small, demonstrating that D-MEIs strongly activate their corresponding neurons. **e**, D-MEI responses plotted versus responses to excitatory and inhibitory D-surround images predicted by an independent static model. This shows that the excitatory and inhibitory D-surround stimuli modulated V1 responses in the direction as predicted by the model. **e**, Finally, we used the above pipeline to optimize MEIs and surround images from example neurons of the MICrONS dataset itself. Schematic shows the MICrONS dataset (left) and MEIs with surround images of four example neurons of the MICrONS dataset are shown on the right. This allows future circuit dissections towards understanding the mechanism underlying center-surround interaction in mouse visual cortex.



**Supplemental Fig. 4. Images restricted to the far surround still result in surround modulation.** **a**, Examples of the MEI, the excitatory surround and cropped excitatory surround. **b**, Examples of the MEI, the inhibitory surround and cropped inhibitory surround. **c**, Comparing predicted response to the MEI, the excitatory surround and the cropped surround image ( $n=3,560$  cells). **d**, Comparing predicted response to the MEI, the inhibitory surround and the cropped surround image ( $n=3,560$  cells). **e**, Comparing observed response to the MEI, the excitatory surround and the cropped surround image ( $n=3,560$  cells). Black dots indicate neurons with significantly higher response under the condition on the y-axis (one-sided Wilcoxon rank-sum test,  $p < 0.05$ , 33.6%, 20.2% and 13.4% significant cells for each pair). Modulation is significant on population level for each pair ( $p$ -value= $1.83 \times 10^{-45}$ ,  $9.98 \times 10^{-45}$ ,  $6.89 \times 10^{-19}$ , Wilcoxon signed rank test). **f**, Comparing observed response to the MEI, the inhibitory surround and the cropped surround image ( $n=3,560$  cells). Black dots indicate neurons with significantly higher response under the condition on the y-axis (one-sided Wilcoxon rank-sum test,  $p < 0.05$ , 55.9%, 40.3% and 19.6% significant cells for each pair). Modulation is significant on population level for each pair ( $p$ -value= $8.05 \times 10^{-73}$ ,  $9.03 \times 10^{-66}$ ,  $2.42 \times 10^{-24}$ , Wilcoxon signed rank test).



**Supplemental Fig. 5. Contrast-matched MEIs result in higher activation than MEIs with excitatory surround.** **a**, Panel shows MEI, excitatory surround with MEI, the contrast-matched MEI, and the difference between the original MEI and the contrast-matched MEI for 4 example neurons. Note that the contrast-matched MEI is a scaled-up version of the original MEI with same features. **b**, Diameters of RFs estimated using sparse noise, the MEIs, the MEIs with excitatory and inhibitory surround, and the contrast-matched MEI. Same data shown in Fig. 2e except for the contrast-matched MEI. The mean of the contrast-matched MEI (magenta distribution) size across all neurons ( $n=4,434$  cells) is  $33.2 \text{ degrees} \pm 0.23$  (mean  $\pm$  s.e.m.). The size of the contrast-matched MEI is slightly larger than the original MEI ( $31.3 \text{ degrees} \pm 0.20$ ). **c**, Model predicted responses to the MEI and excitatory surround (x-axis) and contrast-matched MEI (y-axis). Responses are depicted in arbitrary units, corresponding to the output of the model. **d**, Observed responses to the the MEI and excitatory surround (x-axis) and contrast-matched MEI (y-axis). For each neuron, responses are normalized by the standard deviation of responses to all images. Across the population, the neuronal responses to the contrast-matched MEI was significantly higher ( $p\text{-value}=7.35 \times 10^{-80}$ , Wilcoxon signed rank test, slope of linear regression line=1.58). Across stimulus repetitions, 58.9% of the neurons responded stronger to the contrast-matched MEI ( $n=3$  animals, 560 cells, two-sided t-test,  $p\text{-value}<0.05$ ). Solid line indicates the regression line across the population, and dotted gray line indicates the diagonal. **e**, Contrast comparison between the MEI and excitatory surround (x-axis) and the contrast-matched MEI. By definition, the full-field contrast of each pair of images are matched.



**Supplemental Fig. 6. Surround images extrapolated from the spatial pattern of the MEI.** a, MEIs, surround images extrapolated from the spatial pattern of the MEI and optimized excitatory and inhibitory surround images of example neurons.